

Article

## Global Characterization of CO<sub>2</sub> Column Retrievals from Shortwave-Infrared Satellite Observations of the Orbiting Carbon Observatory-2 Mission

Hartmut Boesch <sup>1,\*</sup>, David Baker <sup>2</sup>, Brian Connor <sup>3</sup>, David Crisp <sup>4</sup> and Charles Miller <sup>4</sup>

<sup>1</sup> Department of Physics & Astronomy, University of Leicester, University Road, Leicester LE1 7RH, UK

<sup>2</sup> Cooperative Institute for Research in the Atmosphere, Colorado State University, Fort Collins, CO 80523, USA; E-Mail: baker@cira.colostate.edu

<sup>3</sup> BC Consulting Limited, Alexandra 9320, New Zealand; E-Mail: bcconsulting@xtra.co.nz

<sup>4</sup> Jet Propulsion Laboratory, California Institute of Technology, 4800 Oak Grove Drive, Pasadena, CA 91109, USA; E-Mails: david.crisp@jpl.nasa.gov (D.C.); charles.e.miller@jpl.nasa.gov (C.M.)

\* Author to whom correspondence should be addressed; E-Mail: hartmut.boesch@le.ac.uk; Tel.: +44-116-252-2273; Fax: +44-116-252-2464.

Received: 7 December 2010; in revised form: 8 February 2011 / Accepted: 9 February 2011 /

Published: 14 February 2011

---

**Abstract:** The global characteristics of retrievals of the column-averaged CO<sub>2</sub> dry air mole fraction, X<sub>CO<sub>2</sub></sub>, from shortwave infrared observations has been studied using the expected measurement performance of the NASA Orbiting Carbon Observatory-2 (OCO-2) mission. This study focuses on X<sub>CO<sub>2</sub></sub> retrieval precision and averaging kernels and their sensitivity to key parameters such as solar zenith angle (SZA), surface pressure, surface type and aerosol optical depth (AOD), for both nadir and sunglint observing modes. Realistic simulations have been carried out and the single sounding retrieval errors for X<sub>CO<sub>2</sub></sub> have been derived from the formal retrieval error covariance matrix under the assumption that the retrieval has converged to the correct answer and that the forward model can adequately describe the measurement. Thus, the retrieval errors presented in this study represent an estimate of the retrieval precision. For nadir observations, we find single-sounding retrieval errors with values typically less than 1 part per million (ppm) over most land surfaces for SZAs less than 70° and up to 2.5 ppm for larger SZAs. Larger errors are found over snow/ice and ocean surfaces due to their low albedo in the spectral regions of the CO<sub>2</sub> absorption bands and, for ocean, also in the O<sub>2</sub> A band. For sunglint observations, errors over the ocean are significantly smaller than in nadir mode with values in the range of 0.3 to 0.6 ppm for

small SZAs which can decrease to values as small as 0.15 for the largest SZAs. The vertical sensitivity of the retrieval that is represented by the column averaging kernel peaks near the surface and exhibits values near unity throughout most of the troposphere for most anticipated scenes. Nadir observations over dark ocean or snow/ice surfaces and observations with large AOD and large SZA show a decreased sensitivity to near-surface CO<sub>2</sub>. All simulations are carried out for a mid-latitude summer atmospheric profile, a given aerosol type and vertical distribution, a constant windspeed for ocean sunglint and by excluding the presence of thin cirrus clouds. The impact of these parameters on averaging kernels and X<sub>CO<sub>2</sub></sub> retrieval errors are studied with sensitivity studies. Systematic biases in retrieved X<sub>CO<sub>2</sub></sub>, as can be introduced by uncertainties in the spectroscopic parameters, instrument calibration or deficiencies in the retrieval algorithm itself, are not included in this study. The presented error estimates will therefore only describe the true retrieval errors once systematic biases are eliminated. It is expected that it will be possible to retrieve X<sub>CO<sub>2</sub></sub> for cloud free observations and for low AOD (here less than 0.3 for the wavelength region of the O<sub>2</sub> A band) with sufficient accuracy for improving CO<sub>2</sub> surface flux estimates and we find that on average 18% to 21% of all observations are sufficiently cloud-free with only few areas suffering from the presence of persistent clouds or high AOD. This results typically in tens of useful observations per 16 day ground track repeat cycle at a 1° × 1° resolution. Averaging observations acquired along ~1° intervals for individual ground tracks will significantly reduce the random component of the errors of the X<sub>CO<sub>2</sub></sub> average product for ingestion into data assimilation/inverse models. If biases in the X<sub>CO<sub>2</sub></sub> retrieval of the order of a few tenth ppm can be successfully removed by validation or by bias-correction in the flux inversion, then it can be expected that OCO-2 X<sub>CO<sub>2</sub></sub> data can lead to tremendous improvements in estimates of CO<sub>2</sub> surface-atmosphere fluxes.

**Keywords:** trace gases; remote sensing; inverse theory

---

## 1. Introduction

Human activities such as fossil fuel combustion and land use change have increased global average atmospheric carbon dioxide (CO<sub>2</sub>) concentrations from a pre-industrial level of 280 parts per million (ppm) to more than 388 ppm as of June 2010. Atmospheric CO<sub>2</sub> acts as an effective greenhouse forcing agent and its increasing concentration has contributed  $1.66 \pm 0.17 \text{ Wm}^{-2}$  to the global radiative forcing [1].

Networks of surface *in situ* CO<sub>2</sub> sensors provide accurate measurements of the globally-averaged atmospheric CO<sub>2</sub> concentration as well as large scale temporal, seasonal, and latitudinal variations. However, these measurements are too sparse to constrain accurate carbon budgets on sub-continental or regional spatial scales leaving key scientific and socio-economic questions about the functioning of the global carbon cycle unresolved [2]. On average about 40 percent of the anthropogenic emissions remain in the atmosphere and 60 percent is taken up by the oceans and terrestrial biosphere. However,

there are large uncertainties associated with the location, strength, distribution and temporal duration of these natural sinks and whether they will persist in the future [3].

Satellite sensors are well-suited to provide dense and uniform atmospheric CO<sub>2</sub> observations over land and ocean on a global scale. Several studies have shown the advantage that space-based CO<sub>2</sub> column observations provide in estimating surface fluxes if they are acquired globally with precisions in the range of 1–10 ppm (0.3–3.0%) and without significant biases [4–9].

In recent years, thermal-infrared (IR) CO<sub>2</sub> measurements from space have become available from the High Resolution Infrared Sounder 2 (HIRS-2) instrument aboard the NOAA 10 satellite, from the Atmospheric Infrared Sounder (AIRS) on the Aqua satellite and from the Infrared Atmospheric Sounding Interferometer (IASI) on METOP. Chedin *et al.* ([10] and references therein) have retrieved mid-tropospheric CO<sub>2</sub> with a precision of around 1% for monthly means averaged over 15° × 15° regions in the tropics that reproduce the seasonal patterns of CO<sub>2</sub> measured by *in situ* aircraft instruments [11]. Several groups have retrieved mid-tropospheric CO<sub>2</sub> with better spatial coverage, spatial resolution and precision using measurements from the AIRS and IASI instrument [12–16]. However, the lack of sensitivity of these thermal-IR data to near-surface CO<sub>2</sub> and potential shortcomings in the description of vertical transport in transport models results in a limited value of these observations for inverse studies of surface fluxes [17,18].

Total CO<sub>2</sub> column data with high near-surface sensitivity can be obtained from shortwave infrared (SWIR) observations. Recently, such measurements have become available through the SCIAMACHY instrument on ENVISAT [19,20]. SCIAMACHY was designed to provide global measurements of trace gases in the troposphere and in the stratosphere, including experimental measurements of CO<sub>2</sub> and CH<sub>4</sub>. Although SCIAMACHY was not optimized for CO<sub>2</sub> observations, CO<sub>2</sub> retrievals from SCIAMACHY have demonstrated a precision approaching ~2% with biases of 1–2% [21–24]. However, as pointed out by Palmer *et al.* [25], the magnitude and variability of the CO<sub>2</sub> columns differs between models and SCIAMACHY, which is most likely due to uncharacterized retrieval and model errors.

The Japanese Aerospace Exploration Agency (JAXA) successfully launched the Greenhouse-gases Observing Satellite (GOSAT) on 23 January 2009. The payload of GOSAT consists of two instruments optimized for observations of atmospheric greenhouse gases: the TANSO-FTS and TANSO-CAI. TANSO-FTS is a Fourier transform spectrometer (FTS) operating in the thermal and shortwave infrared that provides near global measurements of CO<sub>2</sub>, CH<sub>4</sub>, H<sub>2</sub>O, and O<sub>3</sub> [26]. It covers three SWIR bands and one thermal-IR band with spectral resolutions of <0.6 cm<sup>-1</sup> for band 1 and of <0.3 cm<sup>-1</sup> for bands 2–4. The instrument has a field of view of 15.8 mrad which corresponds to a surface footprint with a diameter of 10.5 km at nadir. TANSO-FTS employs a scanning mirror to point the instrument towards a fixed target for the duration of a scan. Over land the scanner will use a flexible scan pattern with 1 to 9 cross track points within ±35° of nadir, yielding a ~750 km cross-track range. From April 2009 through July 2010, the scanner collected 5 cross-track soundings spaced at ~160 km intervals. Since that time, 3 cross-track samples, separated by ~260 km intervals. Over the ocean, within ±20° of the subsolar latitude, the scanner can point the instrument boresight to observe the sunglint spot otherwise the nadir scan mode is used. TANSO-CAI is a cloud and aerosol imager that uses four narrow spectral bands to characterize scattering interferences in the FTS field of view. The first year of GOSAT observations have yielded promising results and the observed global

distributions and seasonal variations are consistent with those of the reference data obtained from ground-based remote-sensing (e.g., [27,28]) and airborne *in situ* instruments [29]. However, initial validation showed that the retrievals of column-averaged dry mole fraction  $X_{CO_2}$  were systematically lower by 2 to 3% than the reference values [30]. Significant improvements can be expected from future releases with improved retrieval algorithms.

The Orbiting Carbon Observatory (OCO), NASA's first satellite sensor dedicated to atmospheric  $CO_2$  measurements was launched from Vandenberg Air Force Base, CA at 4:55 am EST on 24 February 2009. Unfortunately, there was a launch vehicle failure and the satellite was lost. However, in early 2010 NASA initiated formulation of an OCO re-flight mission (now known as OCO-2) for a launch readiness no later than February 2013. OCO-2 will use the OCO instrument and mission design including the same orbit to the extent possible to minimize risk and time required to launch readiness.

The OCO-2 mission is developed specifically to deliver space-based  $X_{CO_2}$  data with the precision, temporal and spatial resolution, and coverage needed to characterize the variability of  $CO_2$  sources and sinks on regional spatial scales and seasonal to inter-annual timescales [31,32]. Its most critical requirement is to measure  $X_{CO_2}$  with 1–2 ppm (0.3–0.5%) precision with no significant biases on regional scales ( $1,000 \times 1,000 \text{ km}^2$ ) at semi-monthly intervals for up to two years. To achieve these goals, the OCO-2 instrument design is optimized to measure the SWIR absorption bands of  $CO_2$  at 1.61 and 2.06  $\mu\text{m}$ , and the  $O_2$  A-band at 0.765  $\mu\text{m}$ , with high spectral resolution and high signal-to-noise. Furthermore, the instrument is designed to observe the Earth surface with a small field of view with an area of  $3 \text{ km}^2$  in nadir ( $\sim 1.8 \text{ mrad}$  instantaneous field of view and 3 Hz sampling) to maximize the number of cloud-free scenes observed.

The OCO-2 sampling strategy employs two science observation modes. In the nadir mode, the instrument boresight points toward the local sub-spacecraft point on the Earth's surface. This mode will provide the highest spatial resolution. Nadir mode is also expected to yield the most reliable data over bright land surfaces and to maximize the number of cloud-free scenes in regions with patchy clouds. In glint mode, the instrument boresight points at the spot on the Earth surface, where sunlight is specularly reflected. Glint mode yields 10–1,000 times more signal over dark ocean surfaces compared to nadir observations. It is important to note that the OCO-2 instrument pointing is accomplished using the spacecraft attitude control system and not a scanning mirror assembly. Therefore, nadir and glint observations were planned for alternating 16 day repeat cycles since the spacecraft lacked sufficient pointing agility to switch rapidly between nadir and glint modes.

In this study, we have analyzed the theoretical retrieval precision and sensitivity of  $X_{CO_2}$  retrievals from space-based observations of OCO-2 of near infrared and shortwave infrared radiances of reflected sunlight from the Earth's surface using performance parameters for the OCO instrument. Specifically, we have studied the characteristics of OCO-2 soundings and their measurement uncertainties, given by an analysis of the OCO "full-physics" forward model for different surface types, surface pressures, aerosol loadings, and solar zenith angle. Aerosol and cloud statistics derived from MODIS and MISR have been examined to determine the spatio-temporal distribution of the OCO-2 measurement errors and to obtain the expected number of cloud-free OCO-2 soundings from which multi-shot measurement errors can be inferred. This study provides the most accurate current estimate of the performance expected for the OCO-2 mission.

## 2. OCO Full Physics Retrieval Algorithm

The OCO full physics retrieval algorithm was developed to retrieve  $X_{\text{CO}_2}$  from a simultaneous fit of the near-infrared  $\text{O}_2$  A Band spectrum at 0.76  $\mu\text{m}$  and the  $\text{CO}_2$  bands at 1.61 and 2.06  $\mu\text{m}$  as measured by the OCO-2 instrument. While the algorithm was developed to retrieve  $X_{\text{CO}_2}$  from OCO and OCO-2 observations, it was designed to be adaptable to analyze data from other instruments for algorithm testing and validation. The OCO algorithm has successfully been used to analyze observations from SCIAMACHY, GOSAT, and ground-based Fourier Transform spectrometers (FTS) [24].

The retrieval algorithm uses an iterative retrieval scheme based on Bayesian optimal estimation [33,34] to estimate a set of atmospheric/surface/instrument parameters, referred to as the state vector  $\mathbf{x}$ , from measured, calibrated spectral radiances. The forward model and inverse method are the main components of the algorithm and have been described in detail previously [24,32]. Below, we highlight the algorithm improvements and modifications for the version used here.

The forward model describes the physics of the measurement process and relates measured radiances to the state vector  $\mathbf{x}$ . It consists of a radiative transfer (RT) model coupled to a model of the solar spectrum to calculate the monochromatic spectrum of light that originates from the sun, passes through the atmosphere, reflects from the Earth's surface or scatters back from the atmosphere, exits at the top of the atmosphere and enters the OCO-2 instrument. The top of atmosphere (TOA) radiances are then passed through the OCO-2 instrument model to simulate the measured radiances at the OCO-2 spectral resolution.

The version of the OCO algorithm used in the present study employs the Radiant RT model, which solves the radiative transfer equation using the adding-Eigenmatrix method [35,36]. Radiant has been fully linearized to provide analytic weighting functions  $\mathbf{K}$  (derivatives of the radiance spectrum  $\mathbf{y}$  with respect to state vector  $\mathbf{x}$ ). This version of Radiant also contains a full bidirectional reflectance distribution function (BRDF) surface reflectance capability, based on the formulations of LIDORT [37] and a pseudo-spherical approximation that treats the solar beam attenuation in a curved spherical-shell atmosphere, whereas atmospheric scattering is treated using a plane-parallel approximation.

The OCO-2 instrument measures only radiation polarized perpendicular to the plane containing the incoming solar beam and the beam entering the instrument. This requires a vector RT model that yields accurate polarized monochromatic spectral radiances. Scalar RT will lead to unacceptably large retrieval errors [38]. The OCO algorithm solves this problem by incorporating a fast 2-orders-of-scattering (2OS) vector radiative transfer code to correct polarization effects [39,40].

The monochromatic TOA spectrum calculated by the Radiant-2OS code is then multiplied with a synthetic solar spectrum, which is calculated with an algorithm based on an empirical list of solar line parameters [G. Toon, private communication]. The solar line list covers the range from 550 to 15,000  $\text{cm}^{-1}$  and is derived from FTS solar spectra: Atmospheric Trace Molecule Spectroscopy (ATMOS), MkIV balloon spectra for the range 550–5,650  $\text{cm}^{-1}$  [41,42], and Kitt Peak ground-based spectra for 5,000–15,000  $\text{cm}^{-1}$  [43,44]. The solar model includes both disk center and disk integrated line lists.

The instrument model convolves the monochromatic radiance spectrum with the instrument lineshape function (ILS). As described in Boesch *et al.* [24], the instrument model can also simulate continuum intensity scaling, zero-level offsets and channeling effects.

A detailed description of the inverse method can be found in Connor *et al.* [34]. Briefly, the inverse method employs the Levenberg-Marquardt modification of the Gauss-Newton method to find the estimate of the state vector  $\hat{\mathbf{x}}$  with the maximum a posteriori probability, given the measurement  $\mathbf{y}$ . The state vector for this study includes a CO<sub>2</sub> profile, an H<sub>2</sub>O profile, a temperature profile, an aerosol extinction profiles, surface pressure, surface albedo and its spectral change for each band, as well as spectral shift and spectral stretch for each band [34]. For sunglint retrievals over ocean, the Cox and Munk [45] BRDF model describes the surface reflectance, and the six surface albedo parameters are replaced with a single windspeed parameter. For this study, we used a model with 12 vertical levels, which results in 61 and 56 state vector elements for nadir and ocean sunglint retrievals, respectively.

The main parameters for the characterization of the X<sub>CO<sub>2</sub></sub> retrieval that are calculated by the retrieval algorithm are the a posteriori X<sub>CO<sub>2</sub></sub> retrieval error (here simply referred to as the retrieval error or retrieval precision) given by the square root of the variance  $\sigma_{X_{CO_2}}$  and the column averaging kernel  $\mathbf{a}_{CO_2}$ .

After the iterative retrieval process has converged to a solution, the error covariance matrix  $\hat{\mathbf{S}}$

$$\hat{\mathbf{S}} = (\mathbf{K}^T \mathbf{S}_e^{-1} \mathbf{K} + \mathbf{S}_a^{-1})^{-1} \quad (1)$$

and the averaging kernel matrix  $\mathbf{A}$

$$\mathbf{A} = \partial \hat{\mathbf{x}} / \partial \mathbf{x} = \hat{\mathbf{S}} \mathbf{K}^T \mathbf{S}_e^{-1} \mathbf{K} \quad (2)$$

are calculated using the *a priori* covariance matrix  $\mathbf{S}_a$  and the measurement covariance matrix  $\mathbf{S}_e$ . X<sub>CO<sub>2</sub></sub> is inferred by averaging the retrieved CO<sub>2</sub> profile, weighted by the pressure weighting function,  $\mathbf{h}$ , such that

$$X_{CO_2} = \mathbf{h}^T \hat{\mathbf{x}} \quad (3)$$

The associated column averaging kernel for a level  $j$  is then given by

$$(\mathbf{a}_{CO_2})_j = \frac{\partial X_{CO_2}}{\partial \mathbf{u}_j} \frac{1}{\mathbf{h}_j} = (\mathbf{h}^T \mathbf{A})_j \frac{1}{\mathbf{h}_j} \quad (4)$$

and the variance of X<sub>CO<sub>2</sub></sub> by

$$\sigma_{X_{CO_2}} = \mathbf{h}^T \hat{\mathbf{S}} \mathbf{h} \quad (5)$$

### 3. Simulation of OCO-2 Soundings

We have simulated OCO-2 radiance spectra using the forward model of the OCO full physics retrieval algorithm for nadir and sunglint observation modes. These simulations have been carried out for a set of geophysical scenarios that cover a large range of values for the parameters surface albedo, aerosol loading, surface pressure and solar zenith angle (SZA). These parameters will have a large impact on the radiance spectra and thus on the expected retrieval errors and averaging kernels. The water vapor, temperature, and CO<sub>2</sub> profiles, as well as the shape of the aerosol extinction profile, the aerosol type, and the windspeed for ocean sunglint mode, are kept constant in order to keep the number

of required simulations small while still capturing the main variations in the  $X_{CO_2}$  retrieval characterization. A sensitivity analysis has been carried out to investigate the sensitivity of the retrieval error and averaging kernels to those parameters that have been kept constant (section 4.2).

For the simulations of land and ocean scenarios in nadir mode, a Lambertian reflecting surface has been employed. Five different surface types have been chosen: ocean, vegetation, desert, snow/ice and savannah. The spectral surface albedos for the vegetation (conifer), desert, and snow/ice types are taken from the ASTER spectral library [46]. A conifer and soil mixture has been used to represent the savannah type. The Lambertian albedo for ocean in nadir mode has been set to 1% for all three spectral bands. To describe ocean reflectance in sunglint mode, a polarizing non-Lambertian Cox and Munk BRDF kernel for a windspeed of 5 m/s has been used. Snow/ice surfaces are also known to show some anisotropy effects which will depend on the snow physical properties [47]. In general, a Lambertian albedo will result in an overestimation of the nadir reflectance and an underestimate of the glint reflectance. For very wet, melting snow, a sunglint effect similar to that of water surfaces is found and a Lambertian surface will represent a poor description of the true surface reflectance. For dry snow, the surface reflectance is smooth and slowly varying, but it shows a significant increase of the surface reflectance for forward scattering with large angles. Thus, we have excluded snow/ice surfaces for glint mode in our study as our assumption of a Lambertian surface reflectance would introduce significant uncertainties.

The atmospheric aerosol profile has been represented by an exponentially-decreasing extinction profile with a scale height of 2 km for a vertically-integrated aerosol optical depth ranging from 0.01 to 0.3 at 0.76  $\mu\text{m}$ . Pre-computed spectral extinction coefficients are used to infer the aerosol optical depth at all other wavelengths. We have used aerosol optical properties (spectral extinction and absorption coefficients and scattering matrix) for a continental type typically found over Northern America in summer (type 4a) from the climatology given in Kahn *et al.* [48]. The optical properties for the spherical components are computed using a polydisperse Mie scattering code [49], those for the non-spherical components such as mineral dust, with a T-matrix code [50]. In addition, we have included a stratospheric aerosol profile based on SAGE-2 measurements. The optical properties of this stratospheric type are for a 75% solution of  $\text{H}_2\text{SO}_4$  with a modified gamma-function size distribution.

The surface pressure has been varied in steps of 100 hPa between 1,000 hPa and 700 hPa. The surface pressure values correspond to the centre of the atmospheric layer grid. If the surface pressure is not in the bottom layer, then the layers below are discarded and the number of vertical atmospheric levels reduced accordingly. The  $\text{CO}_2$  profile is taken from a MATCH/CASA model run [51] and the  $\text{H}_2\text{O}$  and temperature profiles are from the ECWMF ERA 40 dataset, all for mid-latitude summer conditions (Park Falls, July scenario from [34]). The SZA has been varied between 10° and 75° and 85° for nadir and glint modes, respectively. The viewing zenith angle has been set to zero for the nadir mode while for the glint simulations the viewing zenith angle has been set to the value of the SZA. For OCO-2, it has been planned to offset the pointing from the true glint spot to avoid saturation of the detectors. This spacecraft pointing offset will increase with SZA angle with a near zero value at the sub-solar latitude and a value of up to 9.6 degrees for the largest SZAs. As a consequence, OCO-2 will be able to observe the sunglint spot up to a SZA of 85°. This pointing offset has not been taken into account in this study.

A summary over these parameters and their range is given in Table 1.

**Table 1.** Range of parameters used for simulations.

Parameter	Range
Total tropospheric aerosol optical depth	0., 0.01, 0.05, 0.1, 0.15, 0.2, 0.25, 0.3
Solar zenith angle (°)	
Nadir Mode	10, 20, 30, 40, 50, 60, 65, 70, 75, 80, 85
Glint Mode	10, 20, 30, 40, 50, 60, 65, 70, 75
Surface type	Ocean, vegetation, desert, snow/ice (only nadir), savannah
Surface pressure (hPa)	1,000, 900, 800, 700

To simulate the effect of the limited spectral resolution of the OCO-2 instrument, we have convolved the simulated, monochromatic spectra with a Gaussian-shaped ILS with resolving powers of 18,000, 21,000 and 21,000 for the O<sub>2</sub> A-band, the 1.61 μm CO<sub>2</sub> band and the 2.06 μm CO<sub>2</sub> band, respectively. For each band, we have assumed that the spectrum will be sampled by all 1,024 detector pixels.

The measurement noise has been calculated assuming a constant noise component plus one varying as the square root of incident intensity. As illustrated by Figure 1, the scene brightness shows large variations due to changing surface type. In addition, the intensity varies spectrally due to the presence of strong absorption lines. Consequently, the noise will change from spectrum to spectrum as well as within a spectrum. Continuum signal-to-noise values per spectral sample for SZA of 30° and AOD of 0.1 are given in Table 2.

**Figure 1.** Simulated spectra of the O<sub>2</sub> A Band (top), the 1.61 micron CO<sub>2</sub> band (middle) and the 2.06 micron CO<sub>2</sub> band (bottom) for an AOD of 0.1 and a SZA of 30° for the spectral resolution of OCO-2 instrument. Shown is the spectrum for vegetation (solid line), desert (dotted line), snow/ice (dashed line), savannah (dash dotted line) and ocean (dash dot dotted line).

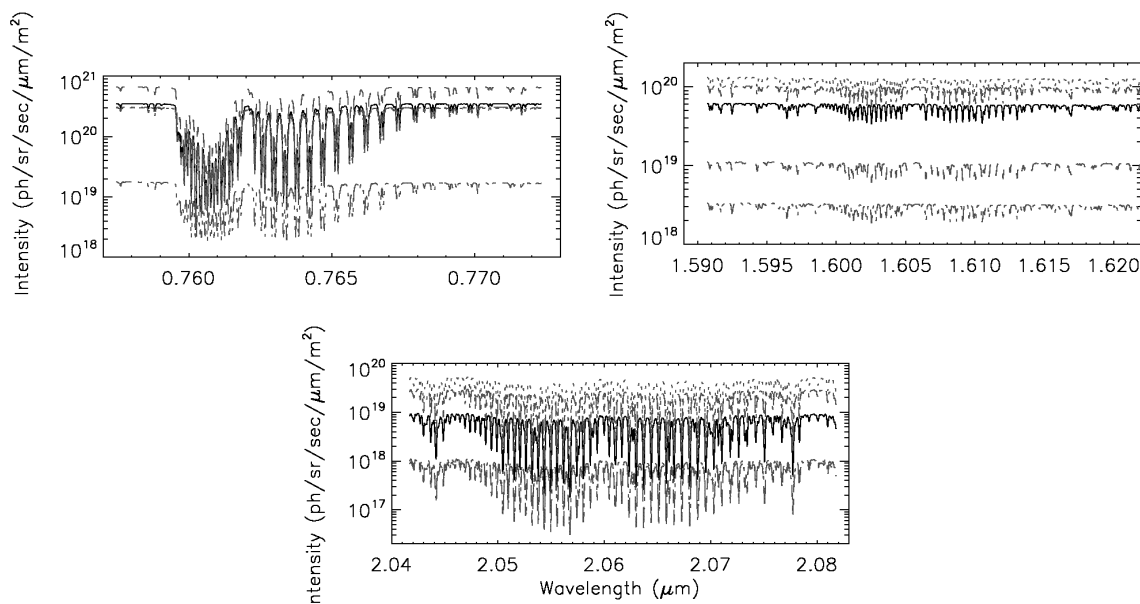
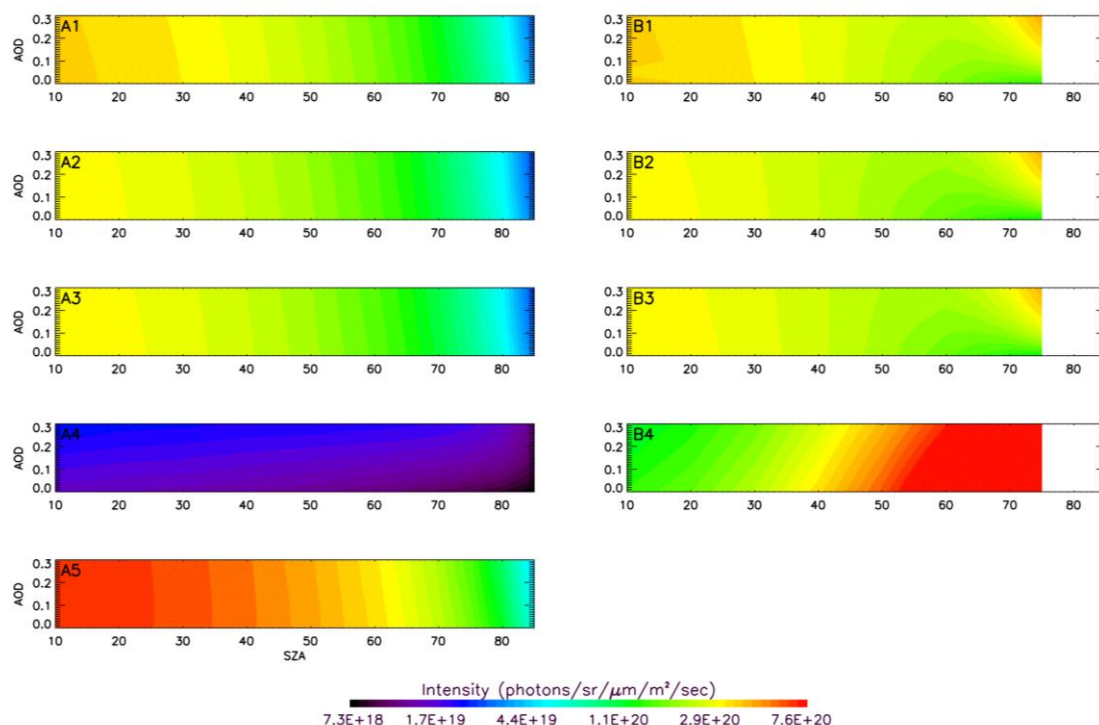


**Table 2.** Continuum Signal-to-Noise Ratio per spectral sample for the 3 OCO-2 channels for the different surface types (SZA = 30 °, AOD = 0.1).

Surface Type	O <sub>2</sub> A-Band	1.61 μm CO <sub>2</sub> Band	2.06 μm CO <sub>2</sub> Band
Ocean	166	81	32
Vegetation	814	440	166
Desert	750	652	448
Snow/ice	1,120	174	28
Savannah	758	570	328

Besides surface albedo, the intensity level, that will directly impact the signal-to-noise ratio, can also change substantially with variations in SZA and AOD. A comparison of the changes in continuum intensity at 0.757 micron with SZA and AOD for nadir and glint geometry for the 5 surface types is shown in Figure 2. In general, the intensity values resemble the reflectivity of the different surfaces,

**Figure 2.** Continuum intensity at 0.757 micron of simulated spectra for nadir (A1–A5) and glint (B1–B4) mode for vegetation (A1/B1), desert (A2/B2), savannah (A3/B3) and ocean (A4/B4) and snow/ice (A5) surfaces.



with very large values being found for snow/ice and low values for ocean in nadir mode. As expected, the continuum intensities decrease with increasing SZA due to the longer atmospheric path and the decreasing value of reflectivity. For SZA less than ~50 °, there is little effect from aerosols for all land surfaces. A more pronounced aerosol effect is visible for ocean in nadir geometry for all SZAs due to the low ocean albedo of 1%. For ocean sunglint, we find a darkening of the scene with increasing aerosol for small SZAs. Furthermore, we can observe a pronounced aerosol effect in sunglint mode over land for large SZAs. The scattering angle in sunglint mode, which is given by approximately the

difference between  $180^\circ$  and twice the SZA, becomes small and the strong forward scattering peak of the aerosol phase functions yields an increase in the observed intensity. Together with the spectra, we have also computed weighting functions for all state vector elements for nadir and sunglint mode, respectively (see section 2). The weighting functions are important quantities for the calculation of the retrieval error (5) and the averaging kernel (2 and 4) which will be discussed in the following section.

#### 4. Characterization of Single-Sounding Errors and Averaging Kernels

##### 4.1. $X_{CO_2}$ Retrieval Errors and Averaging Kernels as a Function of Key Parameters

Given the *a priori* covariance matrix, the simulated weighting functions and the spectral noise, we can calculate the  $X_{CO_2}$  retrieval errors (5) and the column averaging kernels (4) for each simulation. This method is often referred to as linear error analysis and it allows a fast assessment of the retrieval characteristics under the assumption that the retrieval has converged to the correct answer and that the forward model can adequately describe the measurement. It can be thought to give a “best case” error estimate, since any systematic errors in the forward model, that can result from errors in spectroscopic parameters, uncertainties in instrument calibration or in the radiative transfer calculations in the forward model of the retrieval algorithm, must be added to it.

The *a priori* covariance matrices used for this study are described in detail in [34] and they are only briefly summarized here. The *a priori* covariance matrix for  $CO_2$  has been constructed by assuming a root-mean-square (rms) variability of  $X_{CO_2}$  of 12 ppm at the surface with a rapidly decreasing variability with height. The non-diagonal elements of the covariance matrix have been derived from aircraft observations at Carr, CO, USA. For  $H_2O$  and temperature, we have used the observed variability at Park Falls in July. However, for temperature, we have imposed an increasing variability in the lower troposphere to 10 K at the surface. The assumed standard deviation for surface pressure is 20 mbar. The variability of the total aerosol optical depth is  $\pm 0.15$  with a decreasing variability from 150% at the surface to 50% with altitude with a scale height of 2 km and a correlation length of 1 km. The uncertainty in mean albedo is formally set to a value of  $\pm 1$ , with a slope which implies a variation of  $\pm 0.5$  at each end of the spectral range. For ocean sunglint, an uncertainty for windspeed of 1 m/s is used.

The values chosen for the *a priori* covariance matrix will influence to some extent the value for the retrieved  $X_{CO_2}$  and its error estimates. Our approach is to choose *a priori* covariance matrices such that it only imposes a loose constraint on the state vector so that the  $X_{CO_2}$  retrieval errors will be dominated by measurement noise [34]. In general, the measurement is overwhelmingly dominant for albedo, spectral dispersion, and surface pressure. For  $CO_2$ , there is a small *a priori* influence at each altitude which mostly vanishes when calculating the column value  $X_{CO_2}$ . The temperature, water vapour, and aerosol profiles at lower altitudes are reasonably well determined by the measurement, but have a strong *a priori* influence at higher altitudes. It can be expected that minor modifications to the *a priori* covariance matrices will have a negligible effect on the inferred retrieval errors. The effect of substantial modification to the *a priori* covariance matrices, in particular choosing much more constraining matrices, will need to be studied elsewhere.

The  $X_{CO_2}$  retrieval errors obtained are given in Figures 3 and 4 as a function of AOD, SZA, and viewing geometry (nadir/sunglint) for all surfaces and a surface pressure of 1,000 hPa. In nadir mode,

the lowest errors are found for savannah and desert surfaces, with values below 0.5 ppm for SZAs of less than 70°. With increasing SZA, the error increases up to 1.8 ppm for an SZA of 85°. The errors obtained for the vegetation type are only slightly larger, with values of up to 2.5 ppm for the largest SZAs. The retrieval errors obtained for these surfaces in glint mode for SZAs less than ~40° are similar to those obtained in the nadir mode. However, with increasing SZA the errors become significantly larger than for the nadir case. For savannah, desert and vegetation, the largest errors are found for a SZA of 75° with values of up to 1.5 ppm, which is roughly twice as large as in nadir mode.

**Figure 3.** Simulated X<sub>CO2</sub> retrieval error as a function of SZA and AOD for nadir simulations for the five different surface types and a surface pressure of 1,000 hPa.

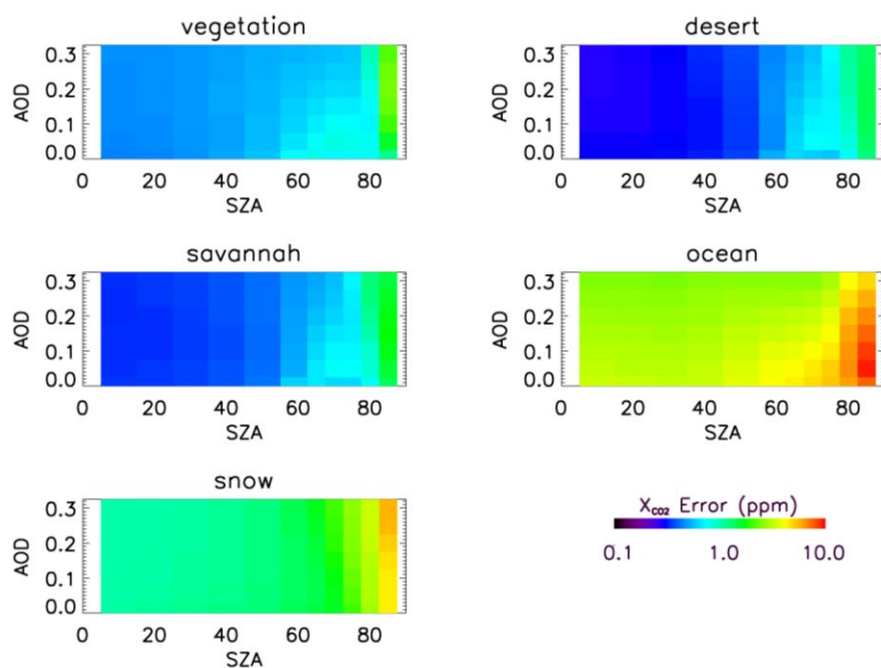
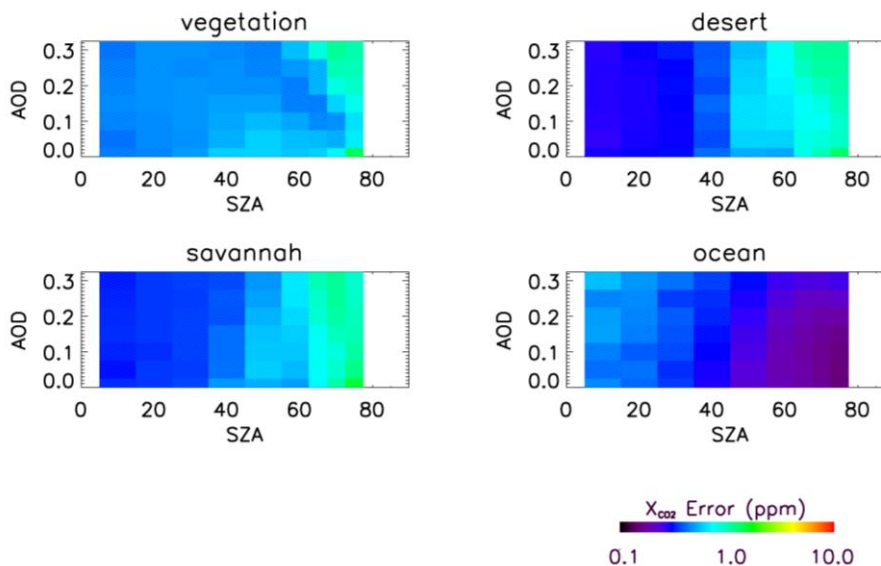


**Figure 4.** Simulated X<sub>CO2</sub> retrieval error as a function of SZA and AOD for glint simulations for the four different surface types and a surface pressure of 1,000 hPa.

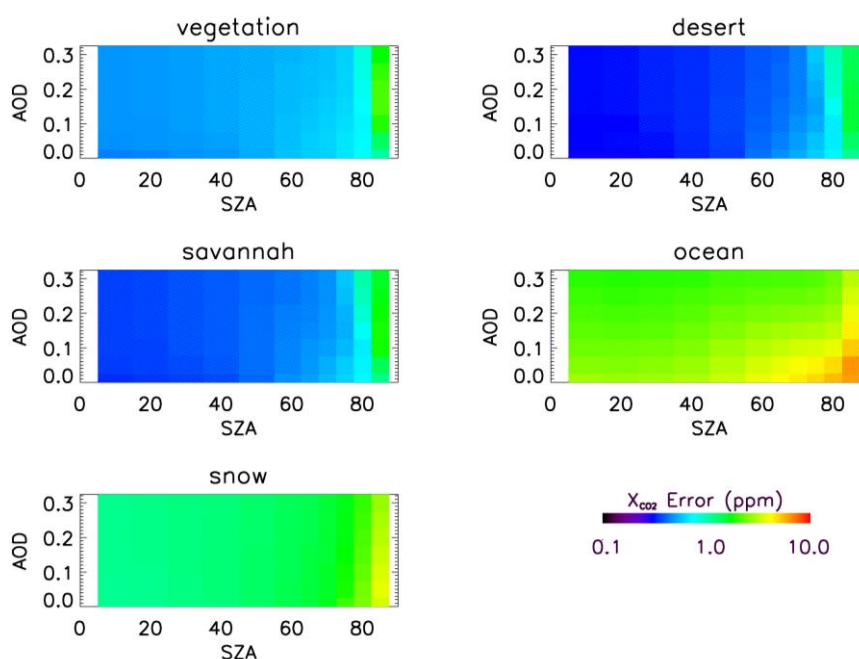


The low surface albedo of snow/ice in the SWIR bands results in substantially higher retrieval errors with values for nadir mode in the range of 1 ppm for small SZAs and up to 6 ppm with increasing SZA.

Very large differences in retrieval errors between the two observations modes are found for the ocean surface. The albedo in nadir mode is low and accordingly the inferred errors are large with values ranging from 2.5 ppm for small SZAs up to 10 ppm for very large SZAs. As a result of the strong sunglint effect over the ocean in sunglint mode, the effective reflectivity is high and subsequently retrieval errors are low. The retrieval errors in ocean sunglint mode are between 0.3 and 0.6 ppm for small SZAs, and decrease with increasing SZA to values as low as 0.15 ppm owing to the large increase in the reflectivity of the sunglint spot.

$X_{CO_2}$  retrieval errors for nadir mode for a surface pressure of 800 hPa are shown in Figure 5. Overall, the  $X_{CO_2}$  retrieval errors are very similar to those obtained for a surface pressure of 1,000 hPa. For very large SZAs, we find that retrieval errors tend to be smaller compared to 1,000 hPa surface pressure, which is most pronounced for ocean and snow/ice. A very similar behavior is observed for the glint mode (not shown), except that retrieval errors for ocean sunglint change very little with surface pressure.

**Figure 5.** Simulated  $X_{CO_2}$  retrieval error as a function of SZA and AOD for nadir simulations for the five different surface types and a surface pressure of 800 hPa.



Figures 6–9 show the corresponding column averaging kernels for nadir and glint mode for a surface pressure of 1,000 hPa and for cases with no tropospheric aerosol and with an AOD of 0.3, which correspond to the minimum and maximum values of AOD included in this study. The averaging kernels for other values of AOD are in-between the cases shown. In nadir mode, the averaging kernels for the four land surface types for SZAs of up to  $40^\circ$  are all very similar, almost independent of the aerosol amount. They are close to unity throughout most of the troposphere and drop off with altitude to a value of  $\sim 0.7$  for a pressure of around 300 hPa. When SZA is increased further, the nadir

averaging kernels for these four land types for conditions without aerosol are still close to unity near the surface, but they drop-off more quickly with altitude, which means that the retrieval loses sensitivity to this altitude range. In the cases with AOD of 0.3, the retrieval loses sensitivity near the surface with increasing SZA, and for very large SZAs we find a clear maximum of the averaging kernel in the mid-troposphere owing to the increasing influence of atmospheric scattering. The somewhat different behavior of the averaging kernels for the uppermost two layers is a result of a differing pressure thickness of these two layers compared to the other layers and we expect that the averaging kernels would show a smooth behavior for strictly equidistant pressure levels.

**Figure 6.** Column averaging kernels (ak) for nadir simulations for different SZAs and the five different surface types with no tropospheric aerosol and a surface pressure of 1,000 hPa.

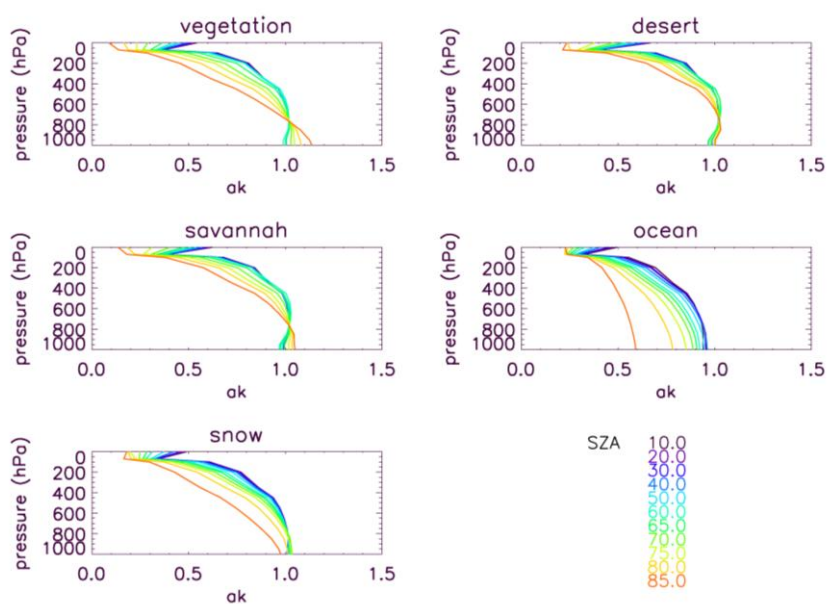


**Figure 7.** Column averaging kernels (ak) for nadir simulations for different SZAs and the five different surface types for an AOD of 0.3 and a surface pressure of 1,000 hPa.

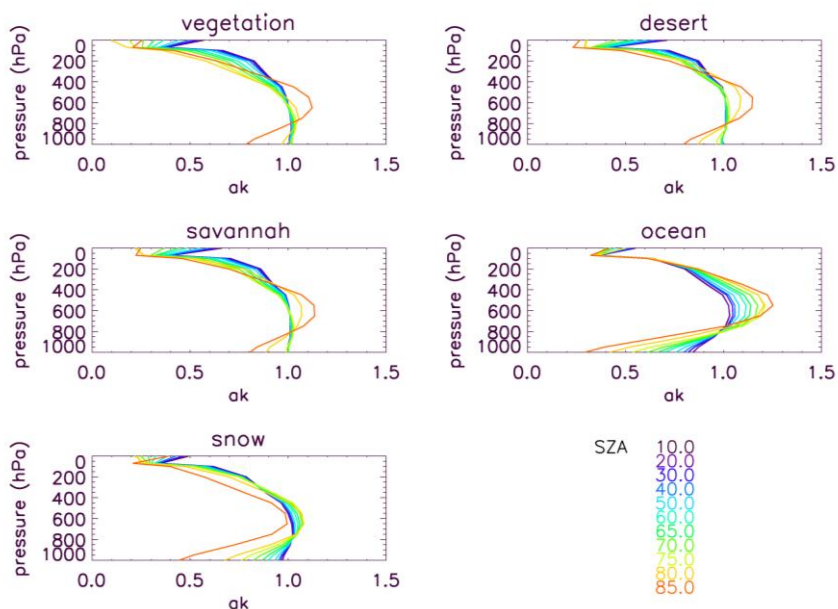


**Figure 8.** Column averaging kernels (ak) for glint simulations for different SZAs and the four different surface types with no tropospheric aerosol and a surface pressure of 1,000 hPa.

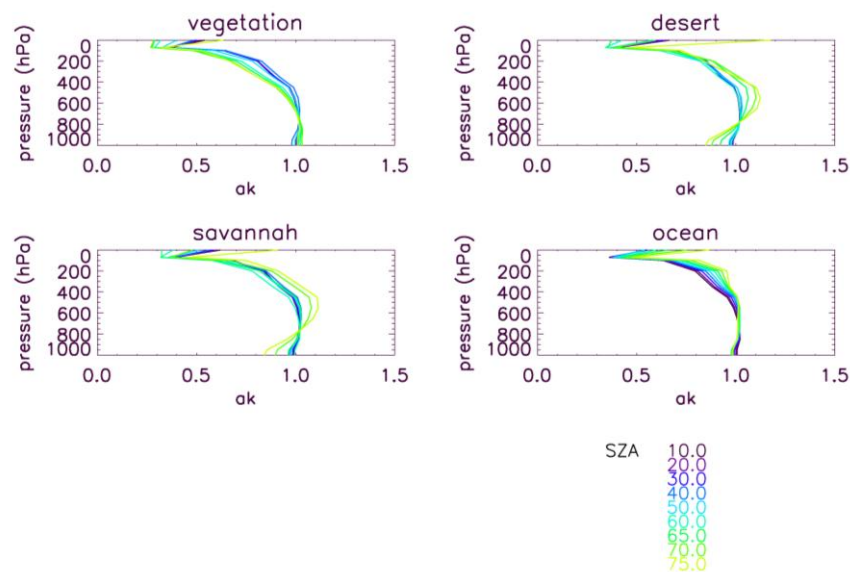
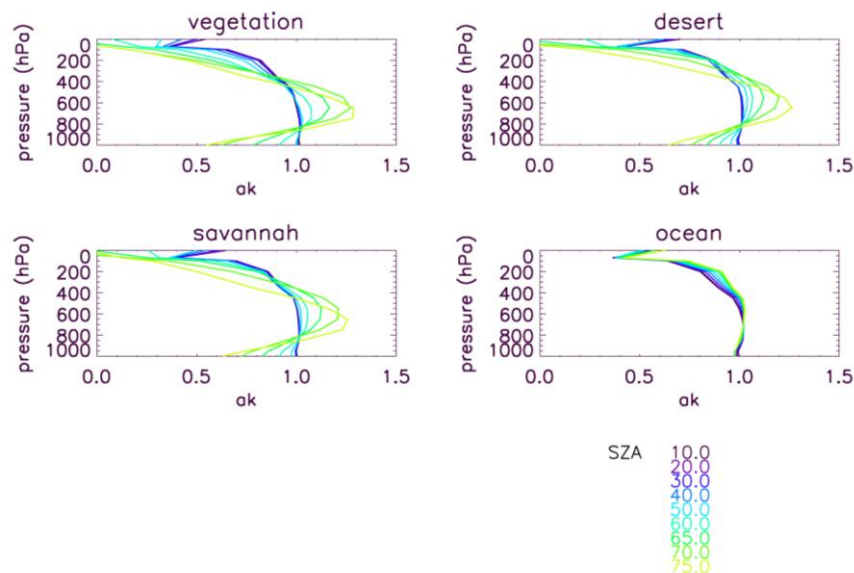


**Figure 9.** Column averaging kernels (ak) for glint simulations for different SZAs and the four different surface types for an AOD of 0.3 and a surface pressure of 1,000 hPa.



In sunglint mode, the averaging kernels for the land surfaces and aerosol-free conditions are almost identical to the nadir kernels for SZAs up to  $40^{\circ}$ – $50^{\circ}$ . With increasing SZA, the averaging kernels for vegetation remain similar to those in nadir mode, whereas for desert and savannah, a maximum of the kernels at  $\sim 500$  hPa is found. For AOD of 0.3, the averaging kernels over land are similar to the nadir kernels only for very small SZAs. The averaging kernels become peaked with increasing SZA with a maximum being found between 500 and 700 hPa.

As for the retrieval errors, there is a large difference in the averaging kernels between nadir and glint mode for ocean surfaces. For small SZAs and aerosol-free conditions, the ocean averaging kernels for nadir and sunglint mode resemble the averaging kernels for land surfaces. However, the

values of the nadir averaging kernels substantially decrease with increasing SZA at all altitudes. In the case of AOD of 0.3, the averaging kernels show a distinct maximum at around 500 hPa even for small SZAs, which becomes more pronounced with increasing SZA. In contrast, the values of the sunglint averaging kernel become large with increasing SZA and they have values close to unity up to 200 hPa for a SZA of 75°. Owing to the large effective reflectivity of the ocean surface in sunglint mode, the averaging kernels are practically insensitive to the aerosol loading.

The nadir averaging kernels for 800 hPa surface pressure for cases with no tropospheric aerosol and with an AOD of 0.3 are shown in Figures 10 and 11. As for the X<sub>CO2</sub> retrieval errors, the averaging kernels for 800 hPa surface pressure are overall similar to those for 1,000 hPa surface pressure. The surface is now located at a lower value for the surface pressure and the averaging kernels appear squeezed compared to those for 1,000 hPa surface pressure. We also find that smaller values for the averaging kernels are smaller for very large SZAs, especially for ocean and snow/ice surfaces.

In summary, the retrieval errors and averaging kernels will substantially vary as a function of geophysical parameters such as surface type or SZA and with observation mode. In nadir mode, the largest retrieval errors are found for large SZAs and dark surfaces such as ocean and snow/ice. In glint mode, the retrieval errors for vegetation, desert and savannah for small and moderate SZAs are similar to those found for nadir mode. The lowest retrieval errors are found over ocean in sunglint mode due to the high specular reflection of the ocean surface. Overall, we find that the effect of aerosols on the retrieval error in nadir and sunglint mode is relatively small except for large SZAs and/or over dark surfaces.

**Figure 10.** Column averaging kernels (ak) for nadir simulations for different SZAs and the five different surface types with no tropospheric aerosol and a surface pressure of 800 hPa.

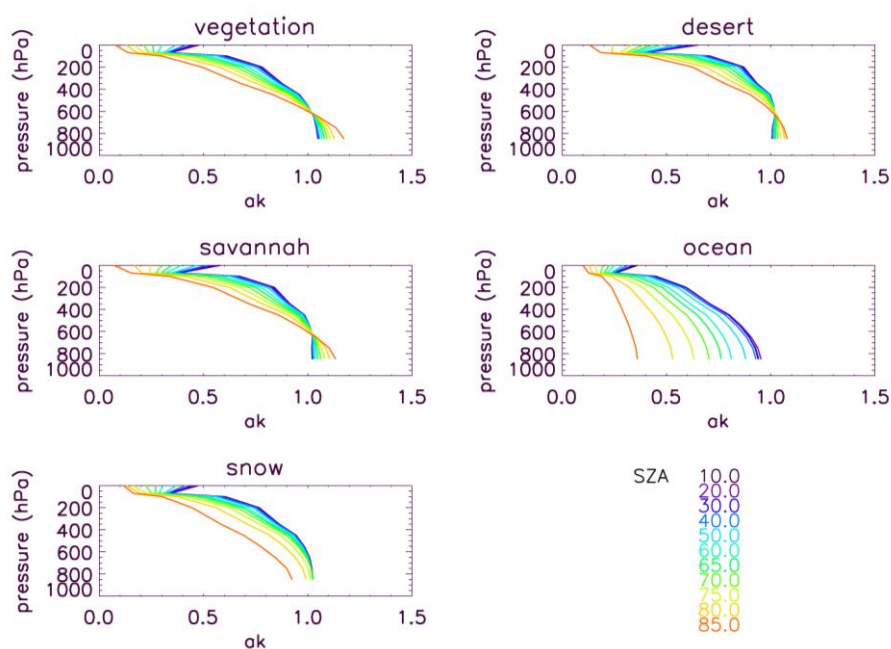
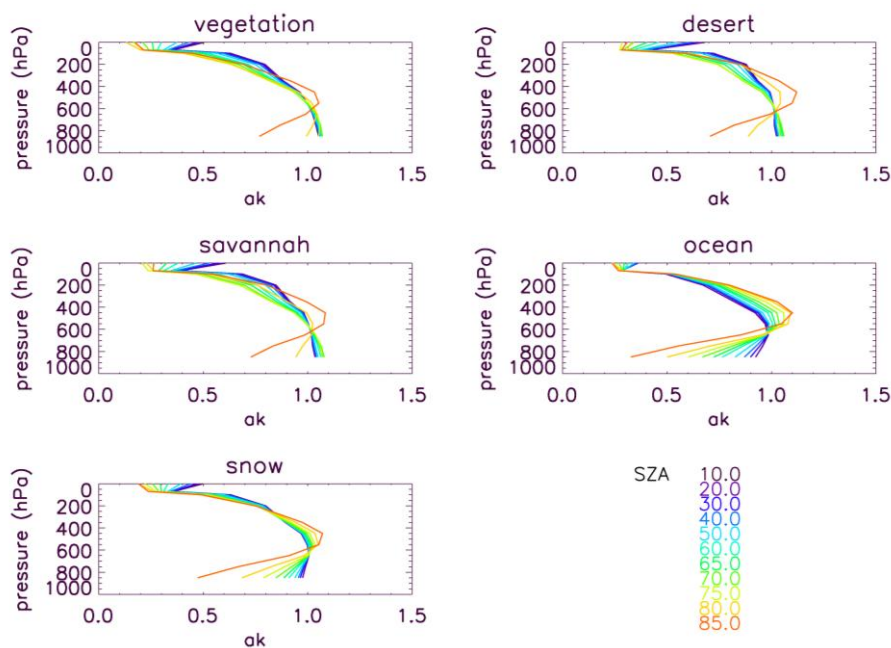


**Figure 11.** Column averaging kernels (ak) for nadir simulations for different SZAs and the five different surface types for an AOD of 0.3 and a surface pressure of 800 hPa.



Nadir column averaging kernels tend to remain close to unity throughout most of the troposphere except for large SZAs and over dark surfaces. For large AODs and SZAs, the averaging kernels tend to show a peak in the mid-troposphere. This behavior is even more pronounced for averaging kernels in glint mode over land. The averaging kernel in sunglint mode over the ocean shows values close to unity almost independent of the aerosol loading. It should be noted that the shape of the averaging kernels for scenarios with a significant aerosol loading will depend somewhat on the assumed aerosol profile and the aerosol type, as is discussed in more detail in section 4.2. Because retrieval errors and averaging kernels depend on the observing geometry, surface type, AOD, and other conditions, which can vary substantially along the ground track, it is essential to use scene-dependent information about averaging kernels and errors for each sounding when estimating surface fluxes from satellite measurements using inversion or data assimilation methods.

#### 4.2. Sensitivity to Other Parameters

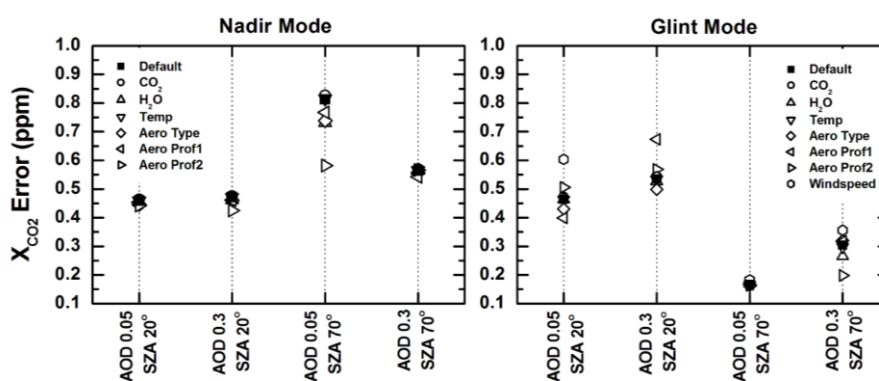
The characterization of single-sounding retrieval errors given in section 4.1 has been inferred for a range of values for surface type, aerosol loading, surface pressure and SZA, while H<sub>2</sub>O, CO<sub>2</sub> and temperature profiles, the shape of the aerosol extinction profile, and the aerosol type have remained constant. In addition, the windspeed for the ocean sunglint mode has been constant. To assess the impact of these assumptions on averaging kernels and X<sub>CO<sub>2</sub></sub> error estimates, we have carried out a series of sensitivity studies for nadir mode over vegetation and sunglint mode over the ocean for SZAs of 20° and 70° and AODs of 0.05 and 0.3.

For each of the above scenarios, the following sensitivity runs have been carried out: (1) add 10 ppm to the CO<sub>2</sub> vmr profile below 550 hPa, (2) double H<sub>2</sub>O vmr below 550 hPa, (3) subtract 10 K from temperature profile below 550 hPa, (4) replace aerosol optical properties with those of type 5b

from Kahn *et al.* [48], (5) replace aerosol extinction profile with a Gaussian shaped profile with 2 km width at (a) 3 km peak altitude or (b) 10 km peak altitude, and (6) add 3m/s to the windspeed for sunglint mode over the ocean.

As can be seen in the comparison of the nadir  $X_{CO_2}$  retrieval errors that are shown in the left panel of Figure 12, only the case with AOD of 0.05 and SZA of  $70^\circ$  shows a significant variability ( $>20\%$ ) in  $X_{CO_2}$  error, with the aerosol-related parameters being the most important followed by water vapour.  $CO_2$  and temperature profile differences seem not to cause any noteworthy variations in  $X_{CO_2}$  errors. For the cases with low SZA and AOD, rather little impact of aerosol-related parameters is expected, as most of the light will come from the dominant surface-reflectance contribution. It is somewhat surprising that for large SZA it is the low AOD case that shows the larger variability of the  $X_{CO_2}$  error. However, in this case, the number of photons being reflected by the surface as well as being scattered in the atmosphere is small. Thus, the weighting between the reflected and scattered contributions will be strongly sensitive to small changes in aerosol scenario which will then alter the retrieval error.

**Figure 12.**  $X_{CO_2}$  retrieval error obtained by the sensitivity studies for nadir mode over vegetation and sunglint mode over the ocean for SZAs of  $20^\circ$  and  $70^\circ$  and AODs of 0.05 and 0.3. The ‘Default’ scenarios refer to the simulations described in section 4.1. The sensitivity tests represent the following scenarios: (1) add 10 ppm to the  $CO_2$  vmr profile below 550 hPa (‘ $CO_2$ ’), (2) double the  $H_2O$  vmr below 550 hPa (‘ $H_2O$ ’), (3) subtract 10 K from temperature profile below 550 hPa (‘Temp’), (4) replace aerosol optical properties with those of type 5b from Kahn *et al.* [48] (‘Aero Type’), (5) replace default aerosol extinction profile with a Gaussian shaped profile with 2 km width at (a) 3 km peak altitude (‘Aero Prof1’) or (b) 10 km peak altitude (‘Aero Prof2’), and (6) add 3m/s to the windspeed for sunglint mode over the ocean (‘Windspeed’).

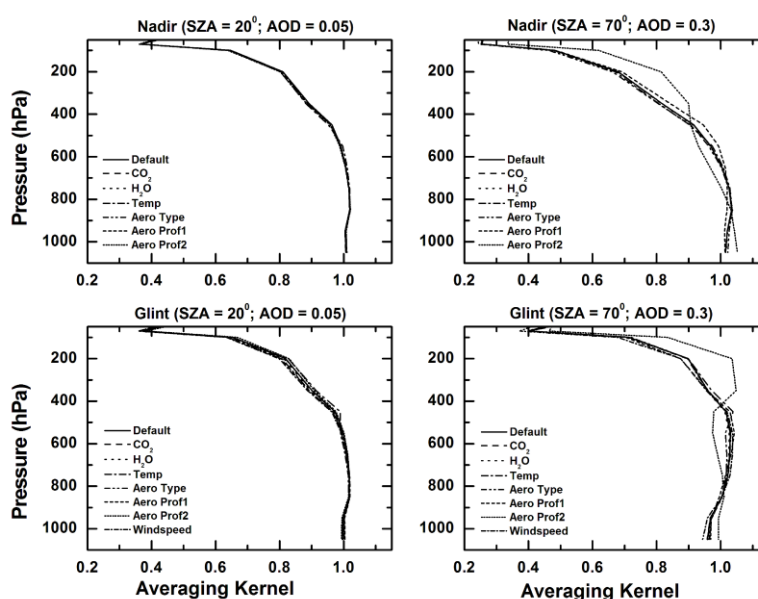


For the sunglint cases (right panel in Figure 12), we find the opposite behavior as for the nadir cases, with the case of SZA of  $70^\circ$  and AOD of 0.05 showing the smallest variability. As discussed earlier, the reflectance of ocean sunglint increases greatly with increasing SZA: for a SZA of  $70^\circ$  the surface signal is very strong, so that the aerosol-related parameters only impact our error estimates for large AODs. Indeed, for an AOD of 0.3 we find a change in the error estimate of more than 30% with the aerosol profile. For small SZAs, the surface contribution is smaller and aerosol-related parameters cause some variability in the retrieval errors even for small AODs.

For the sunglint study, windspeed is included as an additional parameter. Increasing the windspeed will lower the direct reflectance of the surface and thus tend to increase the retrieval error. As shown by Figure 12, for low SZA and low AOD windspeed can cause large variations of almost 30% and is an important parameter, in addition to the aerosol-related parameters.

The averaging kernels for two cases (SZA = 20°/AOD = 0.05 and SZA = 70°/AOD = 0.3) for both nadir and glint mode are shown in Figure 13. With the exception of the high aerosol scenario ('Aero Prof2'), the averaging kernels for all other scenarios are all very similar to the default case. For the cases with high SZA and high AOD, windspeed and other aerosol-related parameters also result in some small variations in the averaging kernels.

**Figure 13.** Column averaging kernels obtained by the sensitivity studies for nadir mode over conifer and sunglint mode over ocean for SZAs of 20° and 70° and AODs of 0.05 and 0.3. The labeling is as in Figure 12.



This sensitivity study has shown that assumptions about aerosol-related parameters in section 4.1 have the most influence on the  $X_{CO_2}$  error estimates and averaging kernels. The assumed height of an aerosol layer is the most critical parameter and our error estimates can be wrong by more than 20% in the presence of a very high aerosol layer (e.g., cirrus clouds). Such an aerosol layer will also significantly change the shape of the averaging kernel. Thus, it is important that the retrieval algorithms applied to SWIR spectra acquired by satellites have the ability to adjust aerosol amount and vertical distribution. For OCO-2, the aerosol information is derived from the  $O_2$  A-band and the strong  $CO_2$  band at 2.06  $\mu m$  (e.g., [31]). Also, this emphasizes again the importance of using scene-dependent averaging kernels and error estimates. Other parameters such as  $CO_2$ , temperature,  $H_2O$  or aerosol type have less impact on the averaging kernels and the  $X_{CO_2}$  retrieval error. For the sunglint mode, windspeed is also an important parameter, which can change the  $X_{CO_2}$  errors by an amount similar to that of the aerosol height.

## 5. Global Distribution of $X_{CO_2}$ Errors

The  $X_{CO_2}$  retrieval errors calculated across a range of parameters can now be used to construct the spatio-temporal distribution of these errors on a global scale for the nadir and sunglint observations modes. This will require information about spatio-temporal distribution of SZA, AOD, surface type and surface pressure. The SZA can be directly calculated for a given location and time as determined by the orbit geometry. For AOD, we have generated a climatology that is described in the next section, together with the assumptions that have been made for surface type and pressure. The resulting global  $X_{CO_2}$  error distribution for individual OCO-2 soundings will then be discussed in the following section.

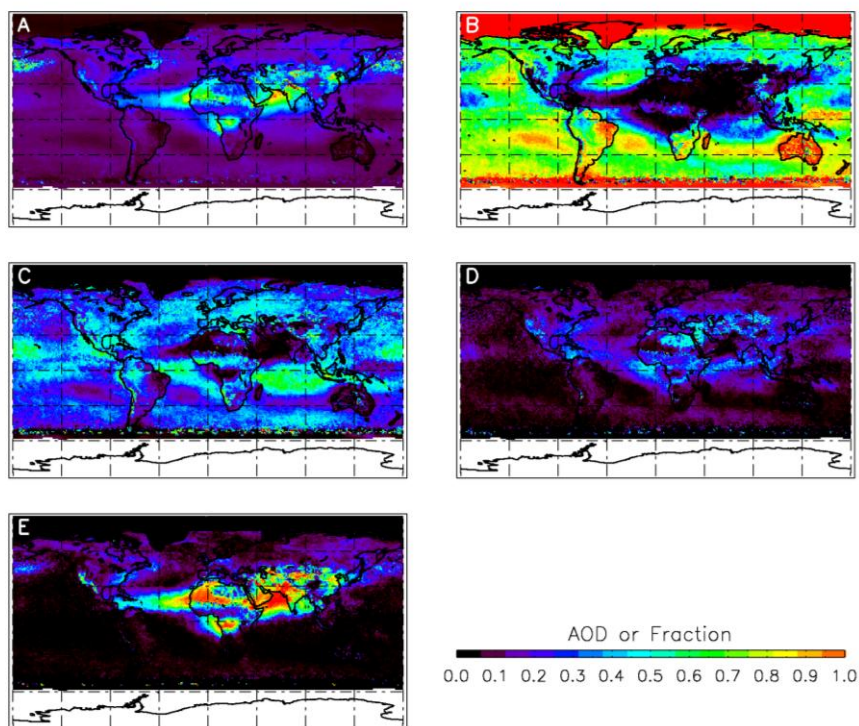
### 5.1. Aerosol and Surface Climatology

We assembled a climatology for AOD for the months of January, April, July and October from the MODIS/Aqua daily L3 product for a 5 year period from 2002 to 2006. The MODIS product gives AOD at 660 nm together with the Angstrom coefficient on a  $1^\circ \times 1^\circ$  grid, which has been used to infer AOD for our reference wavelength of 760 nm. For each of the 4 months and  $1^\circ \times 1^\circ$  grid squares, we have obtained roughly 150 values for AOD from which the probability density function for the four AOD bins [0.0, 0.1], [0.1, 0.2], [0.2, 0.3] and [0.3, inf.] have been calculated. The ability of MODIS to quantify the aerosol optical depth over bright surfaces, such as desert or snow/ice, is limited and often no value is reported in the MODIS data file. To fill such data gaps, we have taken AOD from observations by MISR, a multiple-viewing aerosol/cloud instrument, for desert regions and from model calculations of the NCAR Community Climate Model (CCM3) for snow/ice regions. The MISR Level 3 aerosol product reports AOD at 550 nm and we assumed an Angstrom coefficient of 0.6 to extrapolate to 760 nm. AOD from CCM3 is given for 630 nm and here we have used an Angstrom coefficient of 1.3 to extrapolate. The Angstrom coefficients have been roughly estimated from MODIS observations in the proximity of the snow/ice and desert regions. For simplicity, we have used monthly mean values from MISR and CCM3. To obtain a probability distribution, we have assumed a Gaussian distribution with a FWHM of 70% of the optical depth, a value that has been estimated from the probability distribution based on the daily MODIS data. Thus, the probability density distribution for snow/ice and desert surface will be not very accurate.

The AOD probability density function for the 4 AOD bins and the monthly averaged AOD for the month of July are shown in Figure 14.

The mean AOD given in panel A of Figure 14 demonstrates that a large fraction of the globe has a small AOD, with average values less than 0.2 with a high probability for AODs of less than 0.1 (panel B). Larger values are found for highly polluted regions such as India or China, for the Sahara desert, as well as for Tropical Africa, which is in the peak of its biomass burning season in July. The probability density functions shown in panels B to E indicate that these areas have a very low probability for AOD being less than 0.3 and the probability for AOD exceeding 0.3 can approach 100% for some regions. For the OCO-2 mission, soundings with  $AOD > 0.3$  will not be operationally retrieved, so that few if any soundings might be available for such regions. It should be mentioned that optically thin ice clouds, which are frequently present in the tropical region [52,53] and which can have an impact on the retrieval characteristics (see section 4.2), are not included in this aerosol probability distribution.

**Figure 14.** Mean AOD (panel A) and probability density functions (panels B–D) for July. The probability density function is given for the bins  $[0, 0.1]$ ,  $[0.1, 0.2]$ ,  $[0.2, 0.3]$  and  $[0.3, \text{inf.}]$  in panels B, C, D, and E, respectively.



For surface type, we assembled a static, global map based on the Community Land Model 3.0 (CLM3.0) plant functional types, which has been reduced to the 5 types: ocean, snow/ice, savannah, vegetation and desert [5]. The surface types from CLM 3.0 are specified on a  $0.5^\circ \times 0.5^\circ$  grid, which has been converted here to a  $1^\circ \times 1^\circ$  grid. For mixed land/ocean grids, the land type has been chosen for nadir geometry and vice versa for the glint geometry.

To account for changes in surface pressure due to variations of the surface elevation, we constructed a static, global surface pressure map from the GTOPO30 global digital elevation model. The surface elevations provided by GTOPO30 (at a horizontal grid spacing of 30 arc seconds) have been converted into surface pressure using the hydrostatic equation with a scale height of 7.5 km, which has then been averaged over the  $1^\circ \times 1^\circ$  grid cells. This surface pressure map will represent the average surface pressure for each grid cell. Surface pressure variations due to weather patterns are not taken into account.

### 5.2. Spatio-Temporal Distribution of $X_{CO_2}$ Retrieval Errors

Using the aerosol and surface climatologies, we mapped the calculated retrieval errors in space and time to infer their spatio-temporal distribution. These spatio-temporal distributions have been inferred by making a series of assumptions that have been discussed in the previous section and that are again summarized here: (a) a constant vertical aerosol profile shape and aerosol type has been assumed; (b) a constant atmospheric profile for mid-latitude summer conditions has been used; (c) thin cirrus clouds have been omitted; (d) a constant windspeed for ocean sunglint has been used; (e) Lambertian albedo

for snow/ice has been assumed and (f) spatially and temporally coherent systematic bias in the retrieved  $X_{CO_2}$  have been not included. Results presented in section 4.2 indicate that assumptions (a) to (e) can change the estimated  $X_{CO_2}$  retrieval errors by up to 30% for some geophysical conditions. Also, since spatial and temporal coherent systematic biases (f) in retrieved  $X_{CO_2}$  are not included, these error estimates will only be a good description of the true retrieval errors once such systematic biases are eliminated. Such systematic bias can be due to uncertainties in the spectroscopic parameters and instrument calibration or deficiencies in the physics of the forward model of the retrieval algorithm. Regional scale systematic bias as small as a few tenths of a ppm can have detrimental effects on the retrieval of surface sources and sinks from space-based observations. It will therefore be of critical importance to minimize such biases by rigorous validation and/or by bias-correction schemes in the flux inversion itself. However, a characterization of such systematic error sources is beyond the scope of this paper and needs to be addressed by future studies.

To obtain the spatio-temporal distribution of retrieval error for each OCO-2 sounding we first linearly interpolated the pre-calculated retrieval errors for all AOD values for the surface type for each  $1^\circ \times 1^\circ$  grid cell to the associated surface pressure and the SZA representing that sounding for the 15th of each month. Then an AOD-weighted mean retrieval error was calculated using the aerosol probability distribution function for each grid cell. No retrieval error was been calculated if the SZAs exceeds  $85^\circ$  for nadir soundings and  $75^\circ$  for glint soundings, or if the probability for AOD larger than 0.3 equals unity. For glint mode, we have also excluded areas with snow/ice surfaces. For high mountain areas, such as the Himalayas, there can be surface pressure values lower than the lower limit of 700 hPa used for pre-calculating  $X_{CO_2}$  errors. We have extrapolated the pre-calculated retrieval errors down to values of 650 hPa; no values for the retrieval error will be given for surface pressures smaller than this value. It is to be noted that surface pressure variations due to weather patterns are not taken into account here and the retrieval errors represent mean conditions for a single location and month.

The inferred distribution of retrieval errors for single soundings for January, April, July and October for nadir and glint observation are shown in Figures 15 and 16.

As expected, the most prominent feature for nadir geometry is the large difference of the retrieval errors between ocean (and snow/ice) and land surfaces owing to their largely different surface albedo values. There is also a substantial increase of the errors with increasing SZA that is most pronounced over ocean. Furthermore, the effects of topography can be observed, with somewhat smaller errors being found for higher altitudes. The variability of the retrieval errors as a result of varying aerosol loadings is relatively small. As shown in Figure 14, large aerosol loadings are mostly observed in Tropics and Sub-tropics where the SZAs are typically small, so that the retrieval errors only weakly depend on the aerosol amount (see Figures 3 and 5).

**Figure 15.** Distribution of the  $X_{CO_2}$  retrieval errors for single soundings in nadir mode for January (A), April (B), July (C) and October (D). Data is only shown for SZAs less than  $85^\circ$  and for areas with a surface pressure larger than 650 hPa. It is to be noted that several assumptions have been made when inferring the distribution of the  $X_{CO_2}$  retrieval errors as discussed in the text, most notably not included is the effect of thin cirrus clouds on the  $X_{CO_2}$  retrieval errors and any spatially and temporally coherent systematic bias.

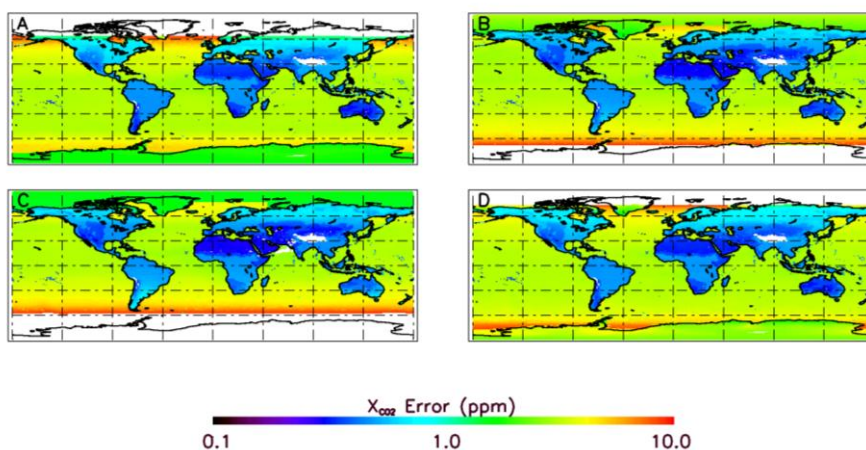
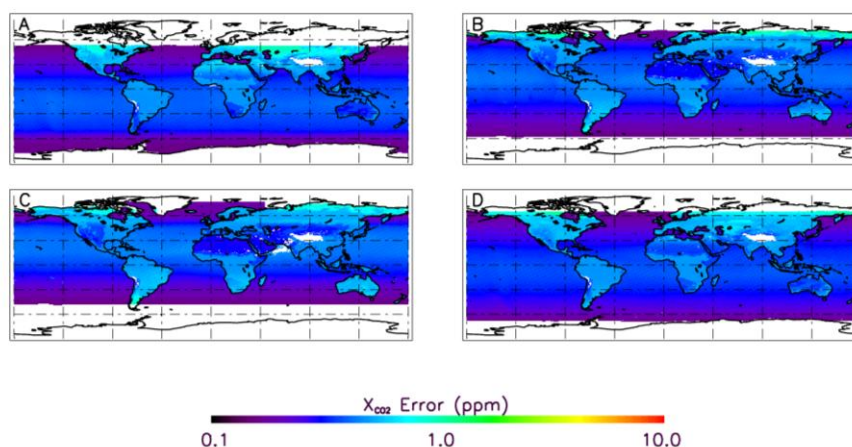


**Figure 16.** Distribution of the  $X_{CO_2}$  retrieval errors for single soundings in glint mode for January (A), April (B), July (C) and October (D). Data is only shown for SZAs less than  $75^\circ$ , snow/ice free conditions and for areas with a surface pressure larger than 650 hPa. It is to be noted that several assumptions have been made when inferring the distribution of the  $X_{CO_2}$  retrieval errors as discussed in the text, most notably not included is the effect of thin cirrus clouds on the  $X_{CO_2}$  retrieval errors and any spatially and temporally coherent systematic bias.



Overall, we find that retrieval errors over land are typically well below 1 ppm for moderate SZAs, but can increase up to 2.5 ppm for very large SZAs. Over ocean and snow/ice, the retrieval errors are typically around 3–4 ppm and can exceed 10 ppm for very large SZAs.

In glint mode, the retrieval errors for land and ocean become similar in magnitude and they typically are in the range of 0.5–1 ppm. The errors over land are slightly larger in glint mode than

those observed for nadir mode. As already discussed in section 4, errors for ocean sunglint decrease with increasing SZA, which is the opposite behavior to that found over land.

## 6. Cloud Climatology and Number of Cloud-Free OCO-2 Soundings

$X_{CO_2}$  will only be retrieved from OCO-2 soundings for scenes which are sufficiently cloud-free to minimize potential biases introduced by clouds. The number of soundings that can be retrieved for a given location and time will thus be determined by the sampling strategy of the satellite instrument and the occurrence of clouds. In the case of the OCO-2 instrument, eight soundings are recorded along a 10-km wide nadir cross-track swath at 3.0 Hz, yielding up to 24 soundings per second and up to 400 soundings per degree of latitude along an orbit track. To reduce the data volume, only four out of the eight cross-track soundings will be transmitted to the ground station and be available for the users. It is planned to fly OCO-2 in the EOS Afternoon Constellation (A-Train) with a 705 km sun-synchronous orbit and equator crossing time between 1:21 pm and 1:30 pm. The A-Train orbit has a 16-day ground track repeat cycle, which allows for complete global  $X_{CO_2}$  coverage twice per month, with  $1.5^\circ$  longitude offsets ( $\sim 150$  km horizontal separation at the equator) between nearby revisits.

We simulated the OCO-2 orbit using the orbital parameters of the Aqua satellite, which has an equator overpass only a few minutes after the OCO-2 satellite. For nadir mode, it has been assumed that the position of the ground pixel falls along the satellite ground track position. In glint mode, the position of the pixel has been inferred by searching for the glint spot for a given satellite position. The observations for all orbits for the months of January, April, July and October with SZAs less than  $85^\circ$  or  $75^\circ$  for nadir or glint mode, respectively, have been added up and binned into  $1^\circ \times 1^\circ$  bins. As mentioned above, it is planned to offset the pointing of OCO-2 from the true glint spot to avoid saturation of the detectors, which has been neglected here.

The number of cloud-free scenes will depend on the size of the ground pixel size of the instrument and the atmospheric path [32,24]. Using the MODIS cloud mask for one day in November, Miller *et al.* [32] estimated that for nadir observations approximately 25% of all soundings are cloud-free for when averaged over the globe for the size of the OCO-2 ground-pixel of  $3 \text{ km}^2$ . Similar results have been found by Breon *et al.* [52], who analyzed GLAS data for an eight week period in autumn of 2003. They have determined that the global fraction of clear-sky scenes with scattering optical depth of less than 0.01 is  $\sim 15\%$  with an additional  $\sim 20\%$  of scenes having total cloud and aerosol optical depth of less than 0.2, the approximate threshold for which accurate  $X_{CO_2}$  retrievals should be possible [31,54,55].

We analyzed 5 years of global MODIS data for January, April, July and October to infer the distribution of the cloud-free fraction. Our analysis uses the monthly mean cloud mask product, which gives the fraction of observed cloud-free scenes for a pixel size of  $1 \text{ km}^2$ . Using the relation between cloud fraction and the size of the ground pixel given in Figure 13 in Miller *et al.* [32], we have transferred this cloud-fraction from MODIS to the OCO-2 ground pixel size.

The observation strategy of OCO-2 will result in a changing ground pixel size during the course of an orbit. OCO-2 will acquire glint and nadir observations with the spectrometer slit oriented perpendicular to the principal plane defined by the sun, surface footprint and the instrument aperture. This approach was adopted to minimize biases associated with polarization of the scene. The

instantaneous field of view (IFOV) of OCO-2 is approx  $1.29 \times 0.1 \text{ km}^2$  and is moved along the orbit track for the duration of the measurement of 1/3 second, which yields a nadir ground pixel with an area between  $1.29 \times 2.26 \text{ km}^2$  if the sun is in flight direction and  $0.1 \times 3.55 \text{ km}^2$  if the sun is perpendicular. For the glint mode, there will be an additional increase of the IFOV due to the non-zero viewing angle

A cloud will impose a significant disturbance not only when it obstructs the field of view of the instrument, but also if it interferes with the incoming solar light, causing cloud shadows. Furthermore, clouds in the proximity of the measurement that do not directly obstruct the incoming solar light or the field of view can still influence the measurement by enhancing the illumination of the apparently cloud-free scene (e.g., [56]). Here, we have assumed that a cloud imposes a significant disturbance when it is located anywhere between the direction of the incoming solar beam and the viewing direction of the instrument, thus the effective area sensitive to clouds could be larger than the ground pixel size itself, depending on the cloud altitude. In this study, we have assumed a cloud height of 5 km which results in an effective area for a SZA of  $75^\circ$  around  $18.5 \times 2.26 \text{ km}^2$  if the sun is in flight direction. For glint mode, the length of the ground pixel in the direction of the sun will then double when assuming that the SZA approximately equals the viewing angle.

Using the effective pixel size, the cloud fraction from MODIS, and the number of soundings from the orbit geometry, the number of cloud free OCO-2 soundings for each  $1^\circ \times 1^\circ$  bin has been calculated assuming that OCO-2 acquires 4 cross track pixels. For OCO-2,  $X_{\text{CO}_2}$  is not routinely retrieved from soundings with  $\text{AOD} > 0.3$  and consequently we have also reduced the cloud free fraction to exclude regions with  $\text{AOD} > 0.3$ . Also excluded are snow/ice regions, as these are problematic regions for MODIS cloud detection.

Figures 17 and 18 show the spatial distribution of cloud-free scenes obtained for nadir and glint mode for the months of January, April, July and October. The observed spatio-temporal distribution of cloud-free OCO-2 soundings follows closely typical large-scale cloud patterns, with a small number of cloud-free soundings being found for the cloudy mid- to high-latitude region. For high latitudes, the number of clear scenes is even more reduced owing to the large SZA for this region and the subsequently larger effective pixel, but as suggested by this study, it should still be possible to find some cloud free soundings within this region. The largest fraction of clear scenes is found in the region between  $30^\circ \text{N}$  and  $30^\circ \text{S}$  with values exceeding 30%. A large variability in the clear sky frequency of this region is imposed by the frequent presence of cirrus clouds and large aerosol amounts, which can result in periods with very few or no cloud-free soundings for some regions such as India. Scenes classified as clear can still include very thin cirrus clouds that are frequently observed in the Tropics. The spatial distribution of  $X_{\text{CO}_2}$  errors shown in section 5.1 does not include such thin cirrus clouds which can have an impact on the  $X_{\text{CO}_2}$  errors and the averaging kernels as discussed in section 4.2. Globally, we find that 18.7%, 20.2%, 20.7% and 19.9% of all soundings are clear in nadir mode for January, April, July and October, respectively. For glint mode, the global fraction of clear scenes is 19.1%, 19.1%, 20.7%, 18.2%.

**Figure 17.** Fraction of cloud-free scenes for nadir observations for January (A), April (B), July (C) and October (D).

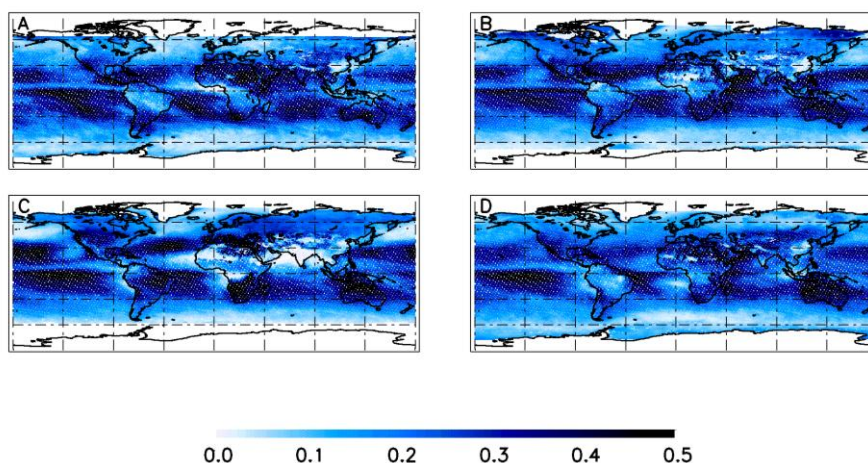
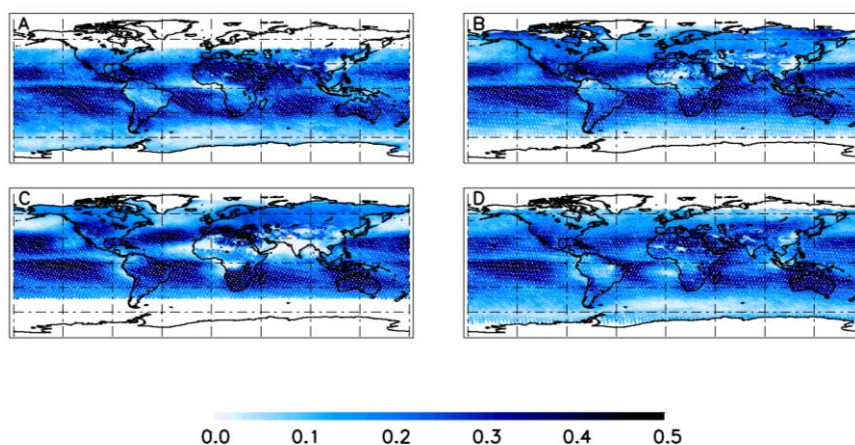


**Figure 18.** Fraction of cloud-free scenes for glint observations for January (A), April (B), July (C) and October (D).



The spatio-temporal distribution of cloud-free soundings for nadir and glint modes are relatively similar with typically smaller values being found for glint mode especially for high latitudes due to the larger effective area. The differences between nadir and glint maps may be somewhat exaggerated at the highest latitudes due to neglecting of the pointing offset of OCO-2. The globally-averaged cloud-free fraction for glint mode is not necessarily smaller than for nadir mode. In glint mode, the instrument points towards the sun so that the number of observations for lower, less cloudy latitudes is increased whereas the number of observations in high, cloudy latitudes is decreased. Furthermore, we have assumed a SZA cutoff for glint mode of  $75^\circ$ , so that less of the cloudy high-latitudes are observed.

## 7. Summary and Discussion

We have studied the global characteristics of  $X_{CO_2}$  retrievals from shortwave infrared satellite observations of the Orbiting Carbon Observatory-2 (OCO-2) mission, which is scheduled for launch in

early 2013. To this end, we have calculated  $X_{CO_2}$  retrieval errors and averaging kernels across a range of surface types, surface pressures, solar zenith angles (SZAs) and aerosol optical depths (AODs), for nadir and sunglint observation modes using the instrumental and orbital characteristics of OCO-2 which have then been mapped in space and time using climatologies for surface pressure, surface type, AOD probability and SZA.

The  $X_{CO_2}$  retrieval errors and the column averaging kernels have been calculated from the *a priori* covariance matrix, the simulated weighting functions and the spectral noise by means of linear error analysis which assumes that the retrieval has converged to the correct answer and that the forward model can adequately describe the measurement. Thus, the inferred errors represent a “best case” error estimate, since any uncorrected systematic biases will have to be added to it.

We have made several assumptions when calculating  $X_{CO_2}$  retrieval errors and the column averaging kernels: (a) a constant vertical aerosol profile shape and aerosol type has been assumed; (b) a constant atmospheric profile for mid-latitude summer conditions has been used; (c) thin cirrus cloud have been not been included; (d) constant windspeed for ocean sunglint has been used; (e) Lambertian albedo for snow/ice surfaces has been assumed and (f) spatially and temporally coherent systematic biases have been not included. The effect of assumptions (a) to (e) have been assessed by a sensitivity study which has shown that aerosol profile and the aerosol type are the most critical parameters for the error estimates. For cases with aerosol layers (or cirrus clouds) in the upper troposphere, our error estimates can be wrong by 20–30% and the shape of the averaging kernels can significantly change. In sunglint mode, the assumed constant windspeed can introduce further uncertainties in our estimates, in particular for low SZA and low AOD. Thus, extending our scheme for the calculation of  $X_{CO_2}$  retrieval errors and averaging kernels to include also variable windspeed and aerosol profiles as well as thin cirrus clouds would lead to some improvements in the characterization of the  $X_{CO_2}$  retrieval, but it would also increase the volume and complexity of the dataset.

We have calculated single-sounding retrieval errors and averaging kernels for nadir and sunglint mode for AODs between 0 and 0.3, for five surface types and surface pressures between 700 and 1000 hPa and for SZAs between  $10^\circ$  and  $85^\circ$  and  $75^\circ$  for nadir and sunglint mode, respectively (Figures 3–5; a subset of the  $X_{CO_2}$  retrieval errors is also given in Tables 3–7). We find that retrieval errors are typically less than 1 ppm for single soundings over most land surfaces for nadir or glint mode for small to moderate SZAs and increase to roughly 3 ppm for large SZAs. For ocean and snow/ice surfaces, the retrieval errors are substantially larger with values as large as 10 ppm for single soundings. The smallest single sounding errors are observed for ocean sunglint mode, with values as small as 0.15 ppm for a SZA of  $75^\circ$ .

In addition to high precision a large near-surface sensitivity of the  $X_{CO_2}$  retrieval is required when using space-based data to constrain surface fluxes. For small to moderate SZAs, the column averaging kernels (Figures 6–11) are typically close to unity throughout most of the troposphere with the largest values being observed near the surface which means that the retrieval captures the whole tropospheric column. With increased SZA, we find that the averaging kernels tend to show increased values in the middle troposphere and decreased values near the surface owing to the increased contribution of atmospheric scattering. This is most pronounced for large AODs, large SZAs and sunglint mode over land where we find values near the surface of around 0.5 so that these soundings will contain reduced information on surface fluxes. How much this effect will impact surface flux inversions from OCO-2

soundings is not clear, but it can be expected to be relatively small as high AOD loads are mostly observed in Tropics/Sub-tropics (Figure 14) where SZAs tend to be small. In sunglint mode over ocean, such a behavior is not observed and the averaging kernels remain close to unity for all SZAs and AODs.

**Table 3.** Calculated  $X_{CO_2}$  retrieval error in ppm for nadir and glint mode for the vegetation surface for a subset of AODs and SZAs for 1000 (800) hPa surface pressure.

AOD/SZA (°)	Nadir Mode				Glint Mode			
	0.0	0.1	0.2	0.3	0.0	0.1	0.2	0.3
10	0.447 (0.445)	0.457 (0.473)	0.463 (0.476)	0.465 (0.474)	0.439 (0.451)	0.450 (0.481)	0.456 (0.450)	0.427 (0.479)
30	0.473 (0.467)	0.481 (0.495)	0.486 (0.498)	0.487 (0.495)	0.491 (0.513)	0.480 (0.495)	0.477 (0.486)	0.472 (0.470)
50	0.572 (0.521)	0.547 (0.532)	0.537 (0.529)	0.525 (0.523)	0.617 (0.590)	0.548 (0.541)	0.468 (0.494)	0.443 (0.461)
70	0.727 (0.592)	0.748 (0.579)	0.630 (0.565)	0.565 (0.553)	0.705 (0.762)	0.471 (0.450)	0.837 (0.480)	1.118 (0.569)
80/75	0.769 (0.755)	0.708 (0.715)	0.796 (0.774)	0.959 (0.832)	1.375 (0.973)	0.646 (0.469)	0.906 (0.458)	1.023 (0.484)
85	1.147 (1.064)	2.023 (1.888)	2.478 (2.137)	2.160 (1.762)	-	-	-	-

**Table 4.** Calculated  $X_{CO_2}$  retrieval error in ppm for nadir and glint mode for the desert surface for a subset of AODs and SZAs for 1000 (800) hPa surface pressure.

AOD/SZA (°)	Nadir Mode				Glint Mode			
	0.0	0.1	0.2	0.3	0.0	0.1	0.2	0.3
10	0.301 (0.296)	0.290 (0.305)	0.283 (0.308)	0.283 (0.309)	0.295 (0.301)	0.280 (0.304)	0.281 (0.303)	0.276 (0.313)
30	0.310 (0.309)	0.300 (0.322)	0.298 (0.325)	0.305 (0.325)	0.310 (0.327)	0.301 (0.325)	0.308 (0.328)	0.319 (0.325)
50	0.356 (0.352)	0.345 (0.361)	0.359 (0.359)	0.372 (0.356)	0.524 (0.426)	0.636 (0.426)	0.618 (0.402)	0.556 (0.371)
70	0.596 (0.521)	0.701 (0.465)	0.623 (0.440)	0.569 (0.445)	0.975 (0.846)	0.766 (0.729)	0.971 (0.823)	1.123 (0.899)
80/75	0.750 (0.707)	0.909 (0.684)	1.035 (0.874)	1.085 (0.976)	1.306 (1.052)	0.891 (0.757)	1.034 (0.755)	1.088 (0.745)
85	1.242 (1.136)	1.420 (1.556)	1.427 (1.485)	1.359 (1.386)	-	-	-	-

**Table 5.** Calculated  $X_{CO_2}$  retrieval error in ppm for nadir and glint mode for the savannah surface for a subset of AODs and SZAs for 1,000 (800) hPa surface pressure.

AOD/SZA (°)	Nadir Mode				Glint Mode			
	0.0	0.1	0.2	0.3	0.0	0.1	0.2	0.3
<b>10</b>	0.342 (0.338)	0.337 (0.355)	0.335 (0.358)	0.336 (0.357)	0.335 (0.346)	0.329 (0.356)	0.332 (0.347)	0.319 (0.362)
<b>30</b>	0.357 (0.355)	0.353 (0.374)	0.354 (0.377)	0.357 (0.376)	0.366 (0.383)	0.355 (0.377)	0.355 (0.376)	0.355 (0.369)
<b>50</b>	0.429 (0.404)	0.407 (0.413)	0.410 (0.410)	0.412 (0.405)	0.530 (0.473)	0.585 (0.461)	0.539 (0.428)	0.474 (0.393)
<b>70</b>	0.630 (0.551)	0.708 (0.505)	0.619 (0.477)	0.561 (0.472)	1.029 (0.809)	0.846 (0.718)	1.051 (0.762)	1.118 (0.819)
<b>80/75</b>	0.769 (0.725)	0.920 (0.689)	1.128 (0.885)	1.253 (1.020)	1.570 (1.067)	1.068 (0.672)	0.958 (0.547)	0.897 (0.533)
<b>85</b>	1.380 (1.156)	1.697 (1.803)	1.729 (1.774)	1.523 (1.592)	-	-	-	-

**Table 6.** Calculated  $X_{CO_2}$  retrieval error in ppm for nadir and glint mode for the ocean surface for a subset of AODs and SZAs for 1,000 (800) hPa surface pressure.

AOD/SZA (°)	Nadir Mode				Glint Mode			
	0.0	0.1	0.2	0.3	0.0	0.1	0.2	0.3
<b>10</b>	3.435 (2.882)	3.126 (2.397)	2.839 (2.121)	2.579 (1.914)	0.464 (0.421)	0.466 (0.445)	0.530 (0.431)	0.620 (0.460)
<b>30</b>	3.296 (2.879)	3.055 (2.425)	2.787 (2.125)	2.528 (1.912)	0.364 (0.359)	0.391 (0.363)	0.421 (0.369)	0.460 (0.374)
<b>50</b>	3.738 (3.395)	3.416 (2.829)	3.024 (2.364)	2.652 (2.049)	0.241 (0.251)	0.273 (0.256)	0.312 (0.262)	0.365 (0.271)
<b>70</b>	4.847 (4.580)	4.153 (3.461)	3.346 (2.602)	2.668 (2.147)	0.163 (0.176)	0.176 (0.178)	0.231 (0.189)	0.304 (0.212)
<b>80/75</b>	6.180 (5.529)	6.411 (3.899)	5.517 (2.839)	4.138 (2.384)	0.149 (0.161)	0.169 (0.166)	0.227 (0.182)	0.285 (0.210)
<b>85</b>	7.899 (6.288)	8.781 (5.311)	6.774 (3.972)	5.033 (3.185)	-	-	-	-

**Table 7.** Calculated  $X_{CO_2}$  retrieval error in ppm for nadir mode for the snow/ice surface for a subset of AODs and SZAs for 1,000 (800) hPa surface pressure.

AOD/SZA (°)	Nadir Mode			
	0.0	0.1	0.2	0.3
<b>10</b>	1.076 (1.132)	1.051 (1.156)	1.036 (1.166)	1.029 (1.163)
<b>30</b>	1.145 (1.193)	1.104 (1.214)	1.084 (1.221)	1.077 (1.216)
<b>50</b>	1.271 (1.335)	1.220 (1.329)	1.210 (1.320)	1.226 (1.304)
<b>70</b>	1.593 (1.655)	1.716 (1.591)	1.899 (1.562)	2.049 (1.537)
<b>80/75</b>	2.927 (2.500)	3.081 (2.299)	3.281 (2.094)	3.406 (1.986)
<b>85</b>	4.441 (3.480)	4.564 (3.579)	5.189 (3.158)	5.778 (2.765)

As expected from the calculated  $X_{CO_2}$  retrievals errors, the spatio-temporal distribution of the calculated single sounding errors shows values well below 1 ppm for most land areas which increase up to 2.5 ppm for very large SZAs (Figures 15 and 16). Specifically, the potential of OCO-2 to improve surface flux estimates for terrestrial ecosystems is demonstrated by the observed smooth distribution of retrieval errors for key regions such as the Tropics or the southern-hemispheric sub-tropics which are poorly observed by surface networks. However, the error estimates for the Tropics can somewhat change when including thin cirrus clouds in the calculation of retrieval errors. OCO-2 should also provide  $X_{CO_2}$  retrievals with high precision over boreal regions during summer months when SZAs are moderate, except for region with snow covered surfaces where retrieval errors would significantly increase.

Much large single sounding random errors are found for nadir observations over dark snow/ice and ocean surfaces. While individual retrievals might be of limited value, OCO-2 collects hundreds of retrievals per degree of latitude along its orbit track, and it might be possible to average these observations to reduce the random error on scales relevant to flux inversion models. The limitation of nadir observations is overcome to a large part by OCO-2's glint mode which is well suited for providing precise  $X_{CO_2}$  retrievals over most of the areas where nadir observations perform very poorly. The estimated precision of the ocean sunglint observations is highest for large SZAs, *i.e.*, for high-latitudes, and thus they provide the potential for precise  $CO_2$  retrievals over areas such as the Southern Ocean, which are of great interest for the ocean carbon cycle [57]. A caveat is that sunglint observations at high latitudes with a large SZA have a very long path through the atmosphere (because the instrument is pointing to the surface at an angle) and therefore obstructions by clouds are very likely.

Glint mode observations over snow/ice surface are not included in this study. Especially, wet, melting snow tends to show a water-like sunglint effect which should lead to small retrieval errors. Such retrievals can be of interest for the determination of clean background conditions and they might warrant a further, more detailed study in the future taking into account BRDF treatment of the surface reflectance.

We find that, globally, between ~18% and ~21% of all OCO-2 observations should be cloud-free (Figures 17 and 18) and that, with very few exceptions for regions with high and persistent aerosol loading, some cloud free observation can be found for a 16 day repeat cycle even over very cloudy areas such as the Southern Ocean. For temporal or spatial ensemble averages of  $X_{CO_2}$  retrievals, it can be expected that random errors would be further reduce with the number of cloud-free retrievals.

The theoretical  $X_{CO_2}$  retrieval error estimates fulfill the OCO-2 requirement to measure  $X_{CO_2}$  with 1–2 ppm (0.3–0.5%) precision already for single-soundings almost everywhere when combining nadir and sunglint soundings and averaging soundings can further reduces these random errors. However, these results represent the theoretical 'best' possible precision that have been inferred by making a series of assumptions as discussed above. Observed variations of a spatial or temporal ensemble of  $X_{CO_2}$  retrievals from measured spectra will typically exceed such theoretical estimates. Small variations in geophysical conditions, such as aerosol distribution or surface albedo, or in instrumental conditions, will lead to scatter in retrieved  $X_{CO_2}$  in addition to scatter due to measurement noise. Such variations are expected to result in a certain level of correlations between retrievals leading to a reduced error reduction for the errors of the ensemble mean.

Furthermore, our  $X_{CO_2}$  retrieval errors do not include systematic biases which can result from errors in spectroscopic parameters, uncertainties in instrument calibration or deficiencies in the radiative transfer calculations in the forward model of the retrieval algorithm. Multiple studies have demonstrated that surface flux inversion are already sensitive to systematic biases in the range of a few tenths of a ppm [5-7,32] and the benefit of OCO-2 observations for improving surface fluxes will depend critically on whether it will be possible to successfully identify, characterize and eliminate such biases by careful validation of the space-based retrievals and by bias-correction methods in the flux inversion schemes.

## 8. Conclusion

We have analyzed the theoretical retrieval precision and sensitivity of  $X_{CO_2}$  retrievals from space-based observations of the forthcoming NASA Orbiting Carbon Observatory-2 (OCO-2) mission which is scheduled for launch early 2013. Specifically, we have studied the characteristics of OCO-2 soundings and their measurement uncertainties, given by an analysis of the OCO “full-physics” forward model for different surface types, aerosol loadings, surface pressures and solar zenith angles.

These simulations have been carried out for a mid-latitude summer atmospheric profile, a given aerosol type and vertical distribution, a constant windspeed for ocean sunglint and by excluding the presence of thin cirrus clouds and we have analyzed the impact of these assumptions on averaging kernels and  $X_{CO_2}$  retrieval errors. The spatio-temporal distribution of the OCO-2 measurement errors and the expected number of cloud-free OCO-2 soundings has been obtained from the aerosol and cloud statistics derived from MODIS and MISR.

We have shown that a measurement strategy combining nadir observations over land with glint observations over ocean, as has been adopted for the OCO-2 mission, yields theoretical estimates for the single sounding  $X_{CO_2}$  retrieval errors in the range of 1 ppm or less almost globally. The vertical sensitivity, which is given by the averaging kernels, is high throughout most of the troposphere with the highest values being typically found near the surface which shows that OCO-2 soundings should be well suited to constrain surface fluxes. For large SZAs and AODs, the near-surface sensitivity is reduced due to an increased contribution from atmospheric scattering.

We show that  $X_{CO_2}$  retrieval errors and averaging kernels can vary substantially from scene to scene and between observations modes which needs to be taken into account when ingesting OCO-2 retrievals into data assimilation/inverse models by using scene-dependent information about averaging kernel and errors that will be provided in the OCO-2 data product.

We have inferred that roughly 20% of all OCO-2 soundings will be cloud-free and we expect to find some cloud-free OCO-2 soundings for most regions except for a few regions with very persistent large AODs values mostly in South East Asia and Africa.

Potential spatially and temporally coherent systematic biases in the  $X_{CO_2}$  retrieval have not been included in our study and they would need to be added to the presented  $X_{CO_2}$  retrieval errors. Undetected, systematic biases, in particular if persistent on regional scales, can have a significant impact on surface flux estimates already for values of the order of a few tenths of ppm and to identify and correct such  $X_{CO_2}$  biases will be one of the key challenges for the OCO-2 mission.

## Acknowledgements

This work was partly performed by the Jet Propulsion Laboratory of the California Institute of Technology, under contract to the National Aeronautics and Space Administration. We gratefully acknowledge Denis O'Brien for use of his orbit simulator and we would like to thank Robert Parker and Austin Cogan for proof-reading. HB is funded by the Research Council UK.

## References

1. Forster, P.; Ramaswamy, V.; Artaxo, P.; Berntsen, T.; Betts, R.; Fahey, D.W.; Haywood, J.; Lean, J.; Lowe, D.C.; Myhre, G.; Nganga, J.; Prinn, R.; Raga, G.; Schulz, M.; Van Dorland, R. Changes in atmospheric constituents and in radiative forcing. In *Climate Change 2007: The Physical Science Basis. Contribution of Working Group I to the Fourth Assessment Report of the Intergovernmental Panel on Climate Change*; Solomon, S., Qin, D., Manning, M., Chen, Z., Marquis, M., Averyt, K.B., Tignor, M., Miller, H.L., Eds.; Cambridge University Press: Cambridge, UK and New York, NY, USA, 2007.
2. Gurney, K.R.; Law, R.M.; Denning, A.S.; Rayner, P.J.; Baker, D.; Bousquet, P.; Bruhwiler, L.; Chen, Y.-H.; Ciais, P.; Fan, S.; *et al.* Towards robust regional estimates of CO<sub>2</sub> sources and sinks using atmospheric transport models. *Nature* **2002**, *415*, 626–629.
3. Le Quere, C.; Raupach, M.R.; Canadell, J.G.; Marland, G.; *et al.* Trends in the sources and sinks of carbon dioxide. *Nature Geoscience* **2009**, *2*, 831–836.
4. Baker, D.F.; Doney, S.C.; Schimel, D.S. Variational data assimilation for atmospheric CO<sub>2</sub>. *Tellus Ser. B* **2006**, *8*, 359–365.
5. Baker, D.F.; Boesch, H.; Doney, S.C.; O'Brien, D.; Schimel, D.S. Carbon source/sink information provided by column CO<sub>2</sub> measurements from the Orbiting Carbon Observatory. *Atmos. Chem. Phys.* **2010**, *10*, 4145–4165.
6. Feng, L.; Palmer, P.I.; Boesch, H.; Dance, S. Estimating surface CO<sub>2</sub> fluxes from space-borne CO<sub>2</sub> dry air mole fraction observations using an ensemble Kalman Filter. *Atmos. Chem. Phys.* **2009**, *9*, 2619–2633.
7. Chevallier, F.; Breon, F.M.; Rayner, P.J. Contribution of the Orbiting Carbon Observatory to the estimation of CO<sub>2</sub> sources and sinks: Theoretical study in a variational data assimilation framework. *J. Geophys. Res.* **2007**, *112*, D09307, doi:10.1029/2006JD007375.
8. Houweling, S.; Hartmann, W.; Aben, I.; Schrijver, H.; Skidmore, J.; Roelofs, G.J.; Breon, F.M. Evidence of systematic errors in SCIAMACHY-observed CO<sub>2</sub> due to aerosols. *Atmos. Chem. Phys.* **2005**, *5*, 3003–3013.
9. Rayner, P.J.; O'Brien, D. The utility of remotely sensed CO<sub>2</sub> concentration data in surface source inversions. *Geophys. Res. Lett.* **2001**, *28*, 175–178.
10. Chedin, A.; Serrar, S.; Scott, N.A.; Crevoisier, C.; Armante, R. First global measurement of midtropospheric CO<sub>2</sub> from NOAA polar satellites: Tropical zone. *J. Geophys. Res.* **2003**, *108*, 4581, doi:10.1029/2003JD003439.
11. Matsueda, H.; Inoue, H.Y.; Ishii, M. Aircraft observation of carbon dioxide at 8–13 km altitude over the western Pacific from 1993 to 1999. *Tellus Ser. B* **2002**, *54*, 1–21.

12. Maddy, E.; Barnet, C.; Goldberg, M.; Sweeney, C.; Liu, X. CO<sub>2</sub> retrievals from the Atmospheric Infrared Sounder: Methodology and validation. *J. Geophys. Res.* **2008**, *113*, D11.
13. Chahine, M.; Barnet, C.; Olsen, E.T.; Chen, L.; Maddy, E. On the determination of atmospheric minor gases by the method of vanishing partial derivatives with application to CO<sub>2</sub>. *Geophys. Res. Lett.* **2005**, *32*, L22803, doi:10.1029/2005GL024165.
14. Engelen, R.J.; McNally, A.P. Estimating atmospheric CO<sub>2</sub> from advanced infrared satellite radiances within an operational fourdimensional variational (4D-Var) data assimilation system: Results and validation. *J. Geophys. Res.* **2005**, *110*, D18305, doi:10.1029/2005JD005982.
15. Crevoisier, C.; Heilliette, S.; Chedin, A.; Serrar, S.; Armante, R.; Scott, N.A. Midtropospheric CO<sub>2</sub> concentration retrieval from AIRS observations in the tropics. *Geophys. Res. Lett.* **2004**, *31*, L17106, doi:10.1029/2004GL020141.
16. Crevoisier, C.; Chédin, A.; Matsueda, H.; Machida, T.; Armante, R.; Scott, N.A. First year of upper tropospheric integrated content of CO<sub>2</sub> from IASI hyperspectral infrared observations. *Atmos. Chem. Phys.* **2009**, *9*, 4797–4810.
17. Chevallier, F.; Fisher, M.; Peylin, P.; Bousquet, S.S.; Breon, F.M.; Chedin, A.; Ciais, P. Inferring CO<sub>2</sub> sources and sinks from satellite observations: Method and application to TOVS data. *J. Geophys. Res.* **2005**, *110*, D24309, doi:10.1029/2005JD006390.
18. Chevallier, F.; Engelen, R.J.; Peylin, P. The contribution of AIRS data to the estimation of CO<sub>2</sub> sources and sinks. *J. Geophys. Res.* **2005**, *32*, L23801, doi:10.1029/2005GL024229.
19. Bovensmann, H.; Burrows, J.P.; Buchwitz, M.; Frerick, J.; Noel, S.; Rozanov, V.V.; Chance, K.V.; Goede, A.P.H. SCIAMACHY: Mission objectives and measurement modes. *J. Atmos. Sci.* **1999**, *56*, 127–150.
20. Burrows, J.P.; Holzle, E.; Goede, A.P.H.; Visser, H.; Fricke, W. SCIAMACHY—Scanning imaging absorption spectrometer for atmospheric chartography. *Acta Astron.* **1995**, *35*, 445–451.
21. Schneising, O.; Buchwitz, M.; Burrows, J.; Bovensmann, H.; Reuter, M.; Notholt, J. Three years of greenhouse gas column-averaged dry air mole fractions retrieved from satellite—Part 1: Carbon dioxide. *Atmos. Chem. Phys.* **2008**, *8*, 3827–3853.
22. Barkley, M.P.; Monks, P.S.; Frieß, U.; Mittermeier, R.L.; Fast, H.; Körner, S.; Heimann, M. Comparisons between SCIAMACHY atmospheric CO<sub>2</sub> retrieved using (FSI) WFM-DOAS to ground based FTIR data and the TM3 chemistry transport model. *Atmos. Chem. Phys.* **2006**, *6*, 4483–4498.
23. Barkley, M.P.; Monks, P.S.; Hewitt, A.J.; Machida, T.; Desai, A.; Vinnichenko, N.; Nakazawa, T.; Yu Arshinov, M.; Fedoseev, N.; Watai, T. Assessing the near surface sensitivity of SCIAMACHY atmospheric CO<sub>2</sub> retrieved using (FSI) WFM-DOAS. *Atmos. Chem. Phys.* **2007**, *7*, 3597–3619.
24. Boesch, H.; Toon, G.C.; Sen, B.; Washenfelder, R.A.; Wennberg, P.O.; Buchwitz, M.; de Beek, R.; Burrows, J.P.; Crisp, D.; Christi, M.; Connor, B.J.; Natraj, V.; Yung, Y.L. Space-based near-infrared CO<sub>2</sub> measurements: Testing the Orbiting Carbon Observatory retrieval algorithm and validation concept using SCIAMACHY observations over Park Falls, Wisconsin. *J. Geophys. Res.* **2006**, *111*, D23.

25. Palmer, P.I.; Barkley, M.P.; Monks, P.S. Interpreting the variability of CO<sub>2</sub> columns over North America using a chemistry transport model: Application to SCIAMACHY data. *Atmos. Chem. Phys. Dis.* **2008**, *8*, 7339–7371.
26. Hamazaki, T.; Kaneko, Y.; Kuze, A.; Kondo, K. Fourier transform spectrometer for Greenhouse Gases Observing Satellite (GOSAT). *Proc. SPIE* **2005**, *5659*, 73–80.
27. Washenfelder, R.A.; Toon, G.C.; Blavier, J.F.; Yang, Z.; Allen, N.T.; Wennberg, P.O.; Vay, S.A.; Matross, D.M.; Daube, B.C. Carbon dioxide column abundances at the Wisconsin Tall Tower site. *J. Geophys. Res.* **2006**, *111*, D22305, doi:10.1029/2006JD007154.
28. Ohyama, H.; Morino, I.; Nagahama, T.; Machida, T.; Suto, H.; Oguma, H.; Sawa, Y.; Matsueda, H.; Sugimoto, N.; Nakane, H.; Nakagawa, K. Column-averaged volume mixing ratio of CO<sub>2</sub> measured with ground-based Fourier transform spectrometer at Tsukuba. *J. Geophys. Res.* **2009**, *114*, D18303, doi:10.1029/2008JD011465.
29. Machida, T.; Matsueda, H.; Sawa, Y.; Nakagawa, Y.; Hirofumi, K.; Kondo, N.; Goto, K.; Nakazawa, T.; Ishikawa, K.; Ogawa, T. Worldwide measurements of atmospheric CO<sub>2</sub> and other trace gas species using commercial airlines. *J. Atmos. Oceanic Technol.* **2008**, *25*, 1744–1754.
30. *Public Release of Concentration Data (Carbon Dioxide and Methane) Analyzed from GOSAT Observational Data*; NIES: Tsukuba, Japan, 2010; Available online: <http://www.gosat.nies.go.jp/eng/result/result.htm> (accessed on 5 March 2010).
31. Crisp, D.; Atlas, R.M.; Breon, F.-M.; Brown, L.R.; Burrows, J.P.; Ciais, P.; Connor, B.J.; Doney, S.C.; Fung, I.Y.; Jacob, D.J.; *et al.* The Orbiting Carbon Observatory (OCO) Mission. *Adv. Space Res.* **2004**, *34*, 700–709.
32. Miller, C.E.; Crisp, D.; Decola, P.L.; Olsen, S.C.; Randerson, J.T.; Michalak, A.M.; Alkhaled, A.; Rayner, P.; Jacob, D.J.; Suntharalingam, P.; Jones, D.B.; *et al.* Precision requirements for space-based XCO<sub>2</sub> data. *J. Geophys. Res.* **2007**, *112*, D10314, doi:10.1029/2006JD007659.
33. Rodgers, C.D. *Inverse Methods for Atmospheric Sounding: Theory and Practice*; World Scientific Publishing Co. Pte. Ltd: Hackensack, NJ, USA, 2000.
34. Connor, B.J.; Boesch, H.; Toon, G.C.; Sen, B.; Miller, C.E.; Crisp, D. Orbiting carbon observatory: Inverse method and prospective error analysis. *J. Geophys. Res.* **2008**, *113*, D05305, doi:10.1029/2006JD008336
35. Spurr, R.; Christi, M. Linearization of the interaction principle: Analytic Jacobians in the “Radiant” model. *J. Quant. Spectrosc. Radiat. Transfer* **2007**, *103*, 431–446.
36. Christi, M.J.; Stephens, G.L. Retrieving profiles of atmospheric CO<sub>2</sub> in clear sky and in the presence of thin cloud using spectroscopy from the near and thermal infrared: A preliminary case study. *J. Geophys. Res.* **2004**, *109*, D04316, doi:10.1029/2003JD004058.
37. Spurr, R.J.D. A new approach to the retrieval of surface properties from earthshine measurements. *J. Quant. Spectrosc. Radiat. Transfer* **2004**, *83*, 15–46.
38. Natraj, V.; Spurr, R.; Boesch, H.; Jiang, Y.; Yung, Y. Evaluation of errors from neglecting polarization in the forward modeling of O-2 A band measurements from space, with relevance to CO<sub>2</sub> column retrieval from polarization-sensitive instruments. *J. Quant. Spectrosc. Radiat. Transfer* **2007**, *103*, 245–259.

39. Natraj, V.; Boesch, H.; Spurr, R.; Yung, Y. Retrieval of X-CO<sub>2</sub> from simulated Orbiting Carbon Observatory measurements using the fast linearized R-2OS radiative transfer model. *J. Geophys. Res.* **2008**, *113*, D11212.
40. Natraj, V.; Spurr, R.J.D. A fast linearized pseudo-spherical two orders of scattering model to account for polarization in vertically inhomogeneous scattering-absorbing media. *J. Quant. Spectrosc. Radiat. Transfer* **2007**, *107*, 263–293.
41. Geller, M. *A High Resolution Atlas of the Infrared Spectrum of the Sun and the Earth Atmosphere from Space, volume III. Key to Identification of Solar Features from 650 to 4,800 cm<sup>-1</sup>*; NASA Reference Publication 122; NASA: Washington, DC, USA, 1992.
42. Geller, M. Line identification in ATMOS solar spectra. In *Laboratory and Astronomical High Resolution Spectra*; Proceedings of ASP Conference No. 81, Brussels, Belgium, 29 August–2 September 1994; ASP Conference Series; Sauval, A.J., Blomme, R., Grevesse, N., Eds.; Astronomical Society of the Pacific: San Francisco, CA, USA, 1995; p. 81.
43. Wallace, L.; Hinkle, K.; Livingston, W.C. *An Atlas of the Photospheric Spectrum from 8,900 to 13,600 cm<sup>-1</sup> (7350 to 11230 Å)*; NSO Technical Report; NSO: Tucson, AZ, USA, 1993.
44. Livingston, W.; Wallace, L. *An Atlas of the Solar Spectrum in the Infrared from 1,850 to 9,000 cm<sup>-1</sup> (1.1 to 5.4 μm)*; NSO Technical Report; NSO: Tucson, AZ, USA, 1991.
45. Cox, C.; Munk, W. Statistics of the sea surface derived from sun glitter. *J. Mar. Res.* **1954**, *13*, 198–227.
46. Baldridge, A.M.; Hook, S.J.; Grove, C.I.; Rivera, G. The ASTER Spectral Library Version 2.0. *Remote Sens. Environ.* **2009**, *113*, 711–715.
47. Arnold, G.T.; Tsay, S.C.; King, M.D.; Li, J.Y.; Soulen, P.F. Airborne spectral measurements of surface–atmosphere anisotropy for arctic sea ice and tundra. *Int. J. Remote Sens.* **2002**, *23*, 3763–3781.
48. Kahn, R.; Banerjee, P.; McDonald, D. Sensitivity of multiangle imaging to natural mixtures of aerosols over ocean. *J. Geophys. Res.* **2001**, *106*, D16.
49. de Rooij, W.A.; van der Stap, C.C.A.H. Expansion of Mie scattering matrices in generalized spherical functions. *Astron. Astrophys.* **1984**, *131*, 237–248.
50. Mishchenko, M.I.; Travis, L.D. Capabilities and limitations of a current Fortran implementation of the T-matrix method for randomly oriented, rotationally symmetric scatterers. *J. Quant. Spectrosc. Radiat. Transfer* **1998**, *60*, 309–324.
51. Olsen, S.C.; Randerson, J.T. Differences between surface and column atmospheric CO<sub>2</sub> and implications for carbon cycle research. *J. Geophys. Res.* **2004**, *109*, D02301, doi:10.1029/2003JD003968.
52. Breon, F.M.; O'Brien, D.; Spinhirne, J.D. Scattering layer statistics from space borne GLAS observations. *Geophys. Res. Lett.* **2005**, *32*, L22802, doi:10.1029/2005GL023825.
53. Eguchi, N.; Yokota, T.; Inoue, G. Characteristics of cirrus clouds from ICESat/GLAS observations. *Geophys. Res. Lett.* **2007**, *34*, L09810, doi:10.1029/2007GL029529.
54. Kuang, Z.; Margolis, J.; Toon, G.; Crisp, D.; Yung, Y. Spaceborne measurements of atmospheric CO<sub>2</sub> by high-resolution NIR spectrometry of reflected sunlight: An introductory study. *Geophys. Res. Lett.* **2002**, *29*, doi:10.1029/2001GL014298.

55. Butz, A.; Hasekamp, O.P.; Frankenberg, C.; Aben, I. Retrievals of atmospheric CO<sub>2</sub> from simulated space-borne measurements of backscattered near-infrared sunlight: Accounting for aerosol effects. *Appl. Opt.* **2009**, *48*, 18, 3322–3336, doi:10.1364/AO.48.00332.
56. Marshak, A.; Wen, G.; Coakley, J.A., Jr.; Remer, L.A.; Loeb, N.G.; Cahalan, R.F. A simple model for the cloud adjacency effect and the apparent bluing of aerosols near clouds. *J. Geophys. Res.* **2008**, *113*, doi:10.1029/2007JD009196.
57. Le Quere, C.; Rödenbeck, C.; Buitenhuis, E.T.; Conway, T.J.; Langenfelds, R.; Gomez, A.; Labuschagne, C.; Ramonet, M.; Nakazawa, T.; Metzl, N.; *et al.* Saturation of the Southern ocean CO<sub>2</sub> sink due to recent climate change. *Science* **2007**, *316*, 1735–1738.

© 2011 by the authors; licensee MDPI, Basel, Switzerland. This article is an open access article distributed under the terms and conditions of the Creative Commons Attribution license (<http://creativecommons.org/licenses/by/3.0/>).